



Novel Hexb-based tools for studying microglia in the CNS

Takahiro Masuda^{1,2,18}✉, Lukas Amann^{1,3,18}, Roman Sankowski^{1,4}, Ori Staszewski^{1,4}, Maximilian Lenz⁵, Paolo d'Errico^{6,7}, Nicolas Snaidero⁸, Marta Joana Costa Jordão¹, Chotima Böttcher¹✉, Katrin Kierdorf^{1,10,11}, Steffen Jung¹², Josef Priller^{9,13,14}, Thomas Misgeld^{8,15,16}, Andreas Vlachos^{5,10}, Melanie Meyer Luehmann^{6,7,10}, Klaus-Peter Knobeloch¹ and Marco Prinz^{1,10,17}✉

Microglia and central nervous system (CNS)-associated macrophages (CAMs), such as perivascular and meningeal macrophages, are implicated in virtually all diseases of the CNS. However, little is known about their cell-type-specific roles in the absence of suitable tools that would allow for functional discrimination between the ontogenetically closely related microglia and CAMs. To develop a new microglia gene targeting model, we first applied massively parallel single-cell analyses to compare microglia and CAM signatures during homeostasis and disease and identified hexosaminidase subunit beta (*Hexb*) as a stably expressed microglia core gene, whereas other microglia core genes were substantially downregulated during pathologies. Next, we generated *Hexb*^{ttdTomato} mice to stably monitor microglia behavior in vivo. Finally, the *Hexb* locus was employed for tamoxifen-inducible Cre-mediated gene manipulation in microglia and for fate mapping of microglia but not CAMs. In sum, we provide valuable new genetic tools to specifically study microglia functions in the CNS.

Tissue-resident myeloid cells in the CNS represent a heterogeneous class of innate immune cells that are essential for the maintenance of organ homeostasis^{1–3}. Among them, parenchymal microglia and CAMs that include perivascular macrophages (pvMΦ) and subdural leptomeningeal macrophages (mMΦ) are the main organ-specific macrophages of the CNS with fundamental roles during steady state and perturbation^{4–7}. The diverse functions of CAMs and microglia are allocated to their distinct locations in the CNS: whereas CAMs are localized at CNS interfaces to control border integrity, parenchymal microglial cells support the function of cortical neurons⁸ and oligodendrocytes in the white matter⁹.

Despite their distinct locations, microglia and CAMs share several lineage-related properties in the healthy CNS, namely their restricted prenatal origin, a longevity accompanied by a robust homeostatic proliferation^{10,11}, and the expression of myeloid cell markers such as ionized calcium binding adaptor molecule (Iba)-1, Cx3 chemokine receptor 1 (Cx3cr1), MER proto-oncogene tyrosine-protein kinase (MerTK), CD11b and the hematopoietic marker CD45 (refs. ^{5,6}). Single-cell transcriptome and proteome profiling as well as advanced imaging technologies have revealed the functional diversity of both parenchymal microglia and CAMs during steady state and perturbation^{12–16}. The different location of parenchymal versus nonparenchymal CNS macrophages in distinct anatomical compartments of the CNS suggests nonredundant functions of these myeloid subtypes, but a clear definition of the

differential functions of CNS myeloid cells has been difficult due to the lack of cell-type-specific targeting tools. In fact, the previously introduced *Cx3cr1*^{Cre} and *Cx3cr1*^{CreERT2} lines target all CNS macrophages and fail to discriminate microglia from CAMs on the genetic level^{10,17,18}. Therefore, experimental approaches using *Cx3cr1*^{GFP}, *Cx3cr1*^{Cre} or *Cx3cr1*^{CreERT2} lines usually assessed a mixture of all CNS macrophages rather than pure microglia populations. In addition, existing transgenic lines such as *Sall1*^{GFP}, *Sall1*^{CreERT2}, *Cx3cr1*^{GFP}, *Cx3cr1*^{Cre} or *Cx3cr1*^{CreERT2} were usually generated based on knockin strategies that may lead to haploinsufficiency or functional knockouts of the respective genes with possible effects on the microglia phenotype.

Consequently, there is an urgent need for new genetic tools to study parenchymal microglia in their physiological setting; that is, the intact organism. Single-cell RNA-sequencing (scRNA-seq) and mass cytometry studies described distinct core signatures for both microglia and CAMs including *Tmem119*, *Siglech*, *Slc2a5*, *P2ry12*, *Fcrls*, *Sal1*, *Hexb*, *Trem2* and others for microglia, whereas CAMs were characterized by high expression of *Lyve1*, *Cd163*, *Siglec1*, *Mrc1* and others^{10–12,15,16,19}.

Here, we first used massively parallel single-cell sequencing to comprehensively characterize the microglial key signature during different pathologies. We found that *Hexb* is a stably expressed microglial gene in several models of neurodegeneration and demyelination. We then applied CRISPR/Cas9 genome editing to develop

¹Institute of Neuropathology, Faculty of Medicine, University of Freiburg, Freiburg, Germany. ²Department of Life Innovation, Graduate School of Pharmaceutical Sciences, Kyushu University, Fukuoka, Japan. ³Faculty of Biology, University of Freiburg, Freiburg, Germany. ⁴Berta-Ottenstein-Programme for Clinician Scientists, Faculty of Medicine, University of Freiburg, Freiburg, Germany. ⁵Department of Neuroanatomy, Institute of Anatomy and Cell Biology, Faculty of Medicine, University of Freiburg, Freiburg, Germany. ⁶Department of Neurology, Medical Center—University of Freiburg, Freiburg, Germany. ⁷Faculty of Medicine, University of Freiburg, Freiburg, Germany. ⁸Institute of Neuronal Cell Biology, Technical University of Munich, Munich, Germany. ⁹Department of Neuropsychiatry and Laboratory of Molecular Psychiatry, Charité—Universitätsmedizin Berlin, Berlin, Germany. ¹⁰Center for Basics in NeuroModulation (NeuroModulBasics), Faculty of Medicine, University of Freiburg, Freiburg, Germany. ¹¹CIBSS—Centre for Integrative Biological Signalling Studies, University of Freiburg, Freiburg, Germany. ¹²Department of Immunology, Weizmann Institute of Science, Rehovot, Israel. ¹³DZNE and BIH, Berlin, Germany. ¹⁴University of Edinburgh and UK DRI, Edinburgh, UK. ¹⁵German Center for Neurodegenerative Diseases, Munich, Germany. ¹⁶Munich Cluster for Systems Neurology, Munich, Germany. ¹⁷Signalling Research Centres BIOSS and CIBSS, University of Freiburg, Freiburg, Germany. ¹⁸These authors contributed equally: Takahiro Masuda, Lukas Amann. ✉e-mail: masuda@phar.kyushu-u.ac.jp; marco.prinz@uniklinik-freiburg.de

two new transgenic mouse models for visualizing and targeting microglia that involve expression of either tdTomato or tamoxifen (TAM)-inducible expression of *Cre* recombinase under the control of the endogenous *Hexb* promoter taking advantage of microglia longevity and self-renewal. Our approach further takes into account previous knowledge showing that there is no replacement of microglia from the circulation in adult animals²⁰. Our newly developed lines are valuable resources for the thorough study of microglial function during development, homeostasis and diseases of the CNS.

Results

Identification of *Hexb* as a stably expressed microglia core gene during pathology. Transcriptomic analyses of microglia using bulk and single-cell approaches have identified a typical microglial transcriptional signature consisting of genes such as *Cx3cr1*, *Csf1r*, *P2ry12*, *Tmem119*, *Gpr34*, *Tgfb1*, *Fcrls*, *Siglech*, *Slc2a5*, *Hexb* and *Sall1* (refs. ^{21–25}). To screen for indicator genes that are stably expressed in microglia during both homeostasis and disease allowing for specific targeting of microglia *in situ*, we used unbiased quantitative scRNA-seq to profile microglia isolated from mouse CNS tissues of four different disease models. First, microglia from brains that underwent either unilateral facial nerve axotomy (FNX) as a model of nontransgenic neurodegeneration, or cuprizone-induced demyelination and remyelination were analyzed as described before (Fig. 1 and Supplementary Fig. 1)¹⁶. In both disease models, the blood-brain barrier remains intact preventing the influx of peripheral myeloid cells and thus allowing for the selective analysis of endogenous microglia and CAMs during pathology²⁰.

Dimensionality reduction using *t*-distributed stochastic neighbor embedding (*t*-SNE) revealed the presence of one main cloud of transcriptionally related homeostatic microglia and separate clouds of disease-associated microglia (Fig. 1a) that involved four main homeostatic clusters (clusters 1–4) and three additional disease-linked microglia clusters (cluster 5 in FNX, and the clusters 6 and 7 in de-/remyelination) (Fig. 1b). Detailed analysis of microglia core genes during homeostasis revealed highest and typically uniform levels of *Hexb*, *Cx3cr1*, *Csf1r* and *P2ry12*, whereas *Tmem119*, *Gpr34*, *Tgfb1*, *Fcrls*, *Siglech*, *Slc2a5* and *Sall1* transcripts were lower or even undetectable among individual microglia (Fig. 1c,d). During pathology, however, particularly *Hexb* was found to be relatively stable expressed even in the disease-related clusters 5–7, whereas the messenger RNA levels of the other typical microglia core genes were all downregulated. Likewise, in symptomatic 5xFAD mice, a transgenic model for Alzheimer's disease, the mRNA levels of both *Hexb* and *Csf1r* were found to be stably expressed by microglia, whereas most of the other genes were downregulated in the Alzheimer's disease-linked microglia clusters (C4–6) (Supplementary Fig. 2).

We next examined transcriptional profiles of individual microglia in the experimental autoimmune encephalomyelitis (EAE) model of multiple sclerosis as described before¹⁵ (Fig. 2). This neuroinflammatory condition is characterized by an influx of multiple immune cells including myeloid cells into the diseased CNS accompanied by different microglia states¹³. We first assembled a transcriptional atlas comprising a total of 3,335 immune cells and represented these data using dimensionality reduction by application of a *t*-SNE plot (Fig. 2a). RaceID analysis then predicted 25 distinct cell clusters (Fig. 2b), containing lymphoid and myeloid cell populations including microglia, CAMs and dendritic cells that were all defined according to their key signature genes (Supplementary Fig. 3). Expression of *Hexb* was restricted to microglia clusters with high expression levels in the homeostatic-microglia-enriched clusters 16 and 17, and the expression levels were lower but still relatively high in the disease-associated microglia-enriched clusters 13, 14, 15 and 18 (Fig. 2b,c,e). In contrast to *Csf1r* mRNA, *Hexb* transcripts were only faintly detected in the other endogenous CNS

macrophage populations, the CAMs. Most other microglia core genes, however, showed low expression levels or were even absent in disease-associated microglia from EAE-sick animals (Fig. 2d,e).

Taken together, our three independent single-cell profiling approaches covering microglia states from four distinct disease conditions revealed that the expression of most of the prototypical microglia signatures genes, including *Tmem119*, *P2ry12*, *Sall1* and *Cx3cr1*, was low during several neurodegenerative and neuroinflammatory conditions with the noticeable exception of *Hexb* that remained permanently detectable in all disease models and is highly restricted to microglia.

***Hexb*^{tdT} mice: a tool to study microglia behavior *in vivo*.** To take advantage of the specific and stable activity of the *Hexb* promoter in microglia, we next targeted the endogenous *Hexb* loci through CRISPR/Cas9-mediated genome editing. In detail, a T2A-tandemTomato (tdT) cassette was knocked in upstream of the *Hexb* stop codon after exon 14, which results in *Hexb*-expressing cells that simultaneously express tdT fluorescent protein (Fig. 3a and Supplementary Fig. 4a). To test whether the insertion of the tdT cassette into the *Hexb* locus affects gene expression pattern in microglia, we performed bulk RNA-seq analysis using microglia isolated from *Hexb*^{tdT} mice compared to wildtype controls. Notably, expression of *Hexb*, as well as *Gfm2* (encoding ribosome-releasing factor 2), the genomic sequence of which overlaps with that of *Hexb* on mouse chromosome 13, was reduced in the *Hexb*^{tdT/+} and *Hexb*^{tdT/tdT} microglia (Supplementary Fig. 5). Similar changes were also observed in *Hexb*^{CreERT2/CreERT2} mice but not in *Hexb*^{CreERT2/+} mice (Supplementary Fig. 5), a new mouse line we describe next. However, microglia from those new mouse lines did not show any further apparent alterations and exhibited very similar gene expression pattern to *Hexb*-wildtype microglia (Supplementary Fig. 5). In contrast, microglia from *Hexb*-deficient (*Hexb*^{−/−}) mice²⁶ showed substantial gene expression differences (Supplementary Fig. 5a,b). These suggested no further off-target effects in our newly generated mouse lines.

To determine the potential of the *Hexb*^{tdT} line to visualize microglia *in situ* we examined parenchymal microglia histologically in several regions of the CNS and found that almost all Iba1⁺ microglia across different CNS regions were labeled in *Hexb*^{tdT/tdT} mice (Fig. 3b–d,f and Supplementary Fig. 4b). Of note, we were unable to detect any ectopic tdT expression in non-Iba1⁺ cells in the CNS, as we did not find double-positive SOX9-expressing astrocytes, NeuN-expressing neurons or adenomatous polyposis coli (APC)-labeled oligodendrocytes (Fig. 3d,f). In sharp contrast to *Cx3cr1*^{GFP/+} mice, perivascular or leptomeningeal CD206⁺ CAMs were labeled to a much lesser extent with tdT in the *Hexb*^{tdT/tdT} line (Fig. 3d–f). Accordingly, colocalization of tdT and green fluorescent protein (GFP) signals was restricted to parenchymal microglia in compound transgenic *Hexb*^{tdT/tdT}*Cx3cr1*^{GFP/+} mice (Fig. 3g). Fluorescence-activated cell sorting (FACS) analysis of cells from the blood, yolk sac and the CNS revealed abundant tdT expression especially in microglia that was developmentally regulated (Fig. 3h,i and Supplementary Fig. 4c), but only small amounts of tdT in CAMs or circulating myeloid cells (Supplementary Fig. 4d). In addition, some F4/80⁺ tissue macrophages in the kidney, but not spleen or liver from *Hexb*^{tdT/tdT} mice were tdT⁺ (Supplementary Fig. 6). Taken together, microglial labeling is highly efficient and specific in the CNS of *Hexb*^{tdT/tdT} mice, but the system targets subsets of peripheral myeloid cells as well.

To investigate the stability and specificity of the tdT signal during CNS pathology, we performed unilateral FNX in *Hexb*^{tdT/+}*Cx3cr1*^{GFP/+} mice and used the unlesioned contralateral facial nucleus as an internal control (Fig. 4a). One week after lesioning, the tdT signal remained restricted to parenchymal microglia in *Hexb*^{tdT/+}*Cx3cr1*^{GFP/+} mice that showed, as expected, an increase in cell

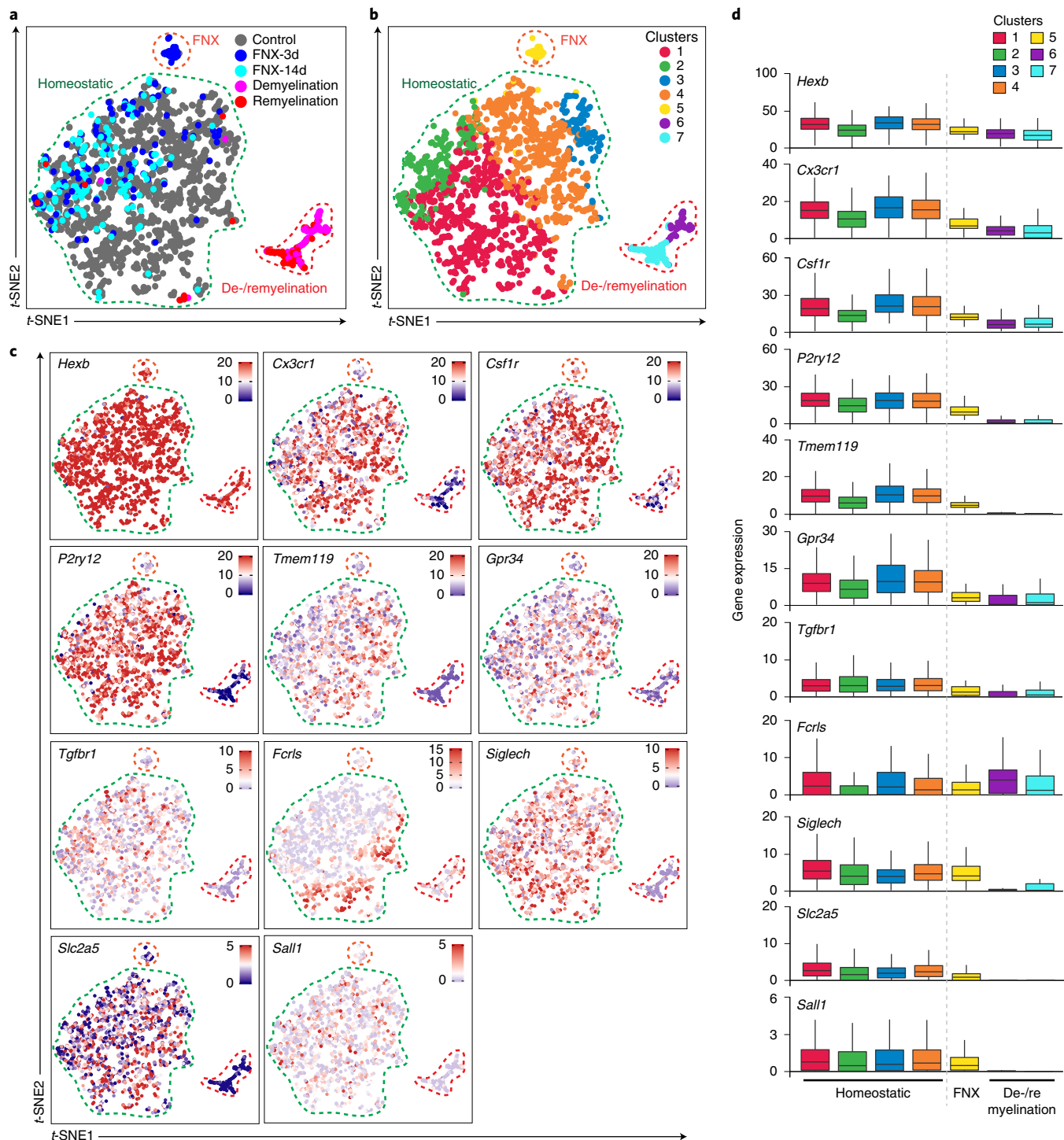


Fig. 1 | scRNA-seq during de- and remyelination and FNX reveals *Hexb* as a stably expressed microglia core gene. **a**, t-SNE plot of 2,242 individual microglia from different conditions. Each dot represents a single cell. Colors correspond to the conditions investigated. Specific disease-associated microglia populations are detectable during demyelination and neurodegeneration. Maps show microglia from either untreated (control) mice or three-dimensional postfacial nerve axotomy (FNX-3D), 14 d post FNX (FNX-14d), cuprizone-induced de- or remyelination. **b**, Seven microglia main clusters depicted on a t-SNE plot ($n=2,242$). Colors represent each cluster. **c**, t-SNE plots depicting expression levels of microglial core genes including *Hexb*, *Cx3cr1*, *Csf1r*, *P2ry12*, *Tmem119*, *Gpr34*, *Tgfb1r*, *Fcrls*, *Siglech*, *Slc2a5* and *Sall1* during different conditions ($n=2,242$). The color key indicates the expression levels. **d**, Box plots exhibit the expression levels of microglial core genes in microglia on a single-cell level in each cluster. The box represents the distribution of 50% single microglia cells for each cluster, and each whisker represents distribution of 25% single microglia. Horizontal lines represent the median gene expression. Colors correspond to the clusters shown in **b**.

number only on the lesioned ipsilateral side (Fig. 4a,b). Expression of tdT was only rarely found on CD206⁺ CAMs, including pvMΦ and mMΦ, or other CNS cells (Fig. 4a), highlighting stable

microglial *Hexb* expression during neurodegeneration. Likewise, in the EAE model of autoimmune CNS inflammation, tdT expression was limited to Iba1⁺CD206⁻ parenchymal cells, whereas

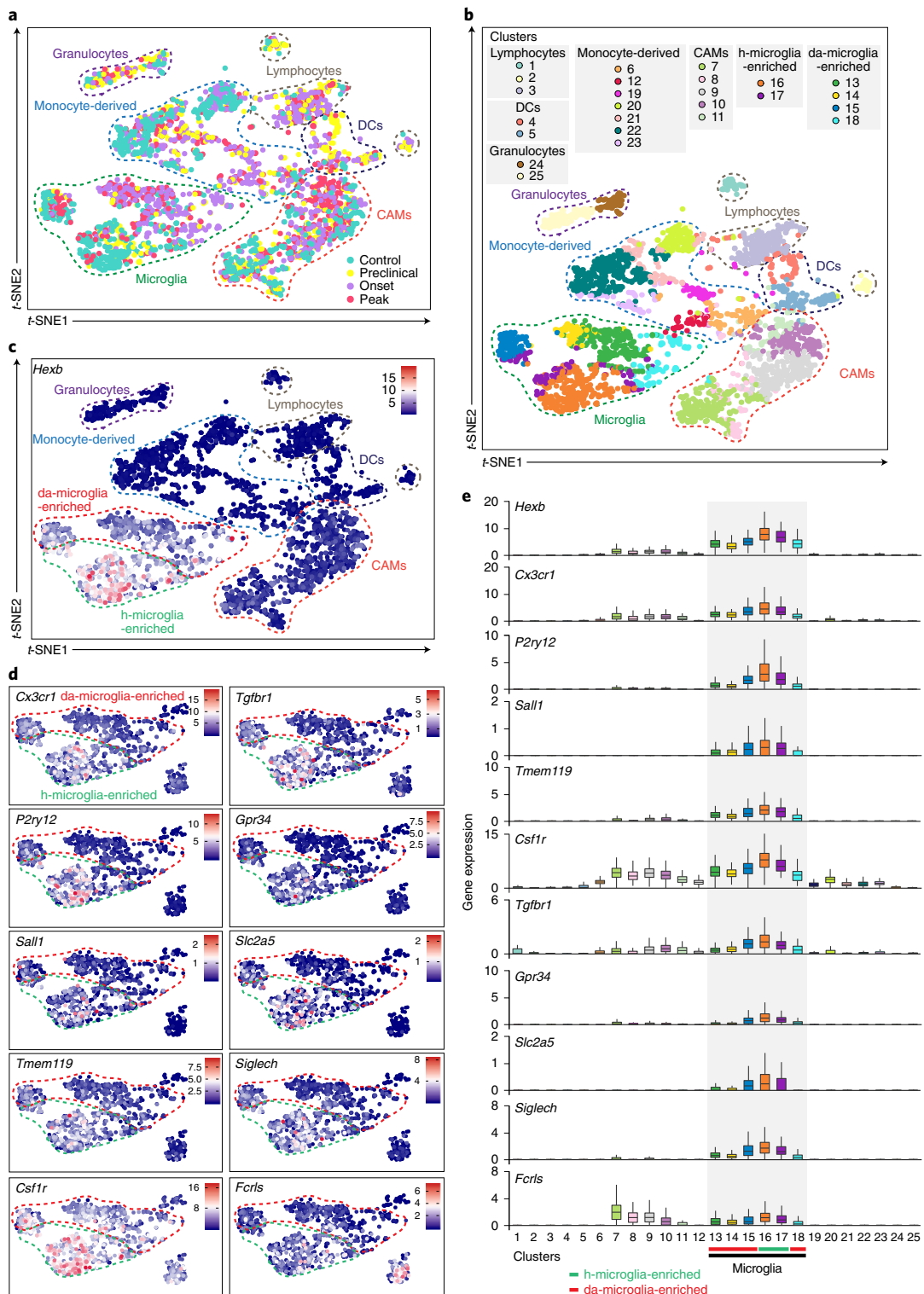


Fig. 2 | Steady high expression of *Hexb* in microglia but not CAMs during homeostasis and autoimmune neuroinflammatory conditions. **a**, t-SNE representation of 3,335 individual hematopoietic cells including microglia, CAMs, monocyte-derived cells, granulocytes, lymphocytes and dendritic cells (DCs), isolated from the spinal cord during either homeostatic condition (control) or different EAE stages (preclinical, onset or peak). Each dot represents a single cell. Colors correspond to the different stages of EAE investigated. Dashed lines indicate different hematopoietic populations. **b**, t-SNE plot illustrating clustering among the hematopoietic populations. Each dot represents a single cell ($n=3,335$). h-microglia enriched, healthy microglia enriched; da-microglia enriched, disease-associated microglia enriched. Colors represent each cluster. **c**, t-SNE plot showing the expression level of *Hexb* across all hematopoietic cells during healthy conditions and neuroinflammation ($n=3,335$). Color key indicates the expression level. **d**, t-SNE map displaying the levels of microglia core genes in h- and da-microglia-enriched clusters. Each dot represents a single cell ($n=925$). Color key indicates the expression level. **e**, Box plots depict the expression levels of microglial core genes across all hematopoietic in microglia on a single-cell level in each cluster. The box represents the distribution of 50% single microglia cells for each cluster, and each whisker represents distribution of 25% single microglia. Horizontal lines represent the median gene expression. Colors correspond to the clusters shown in **b**.

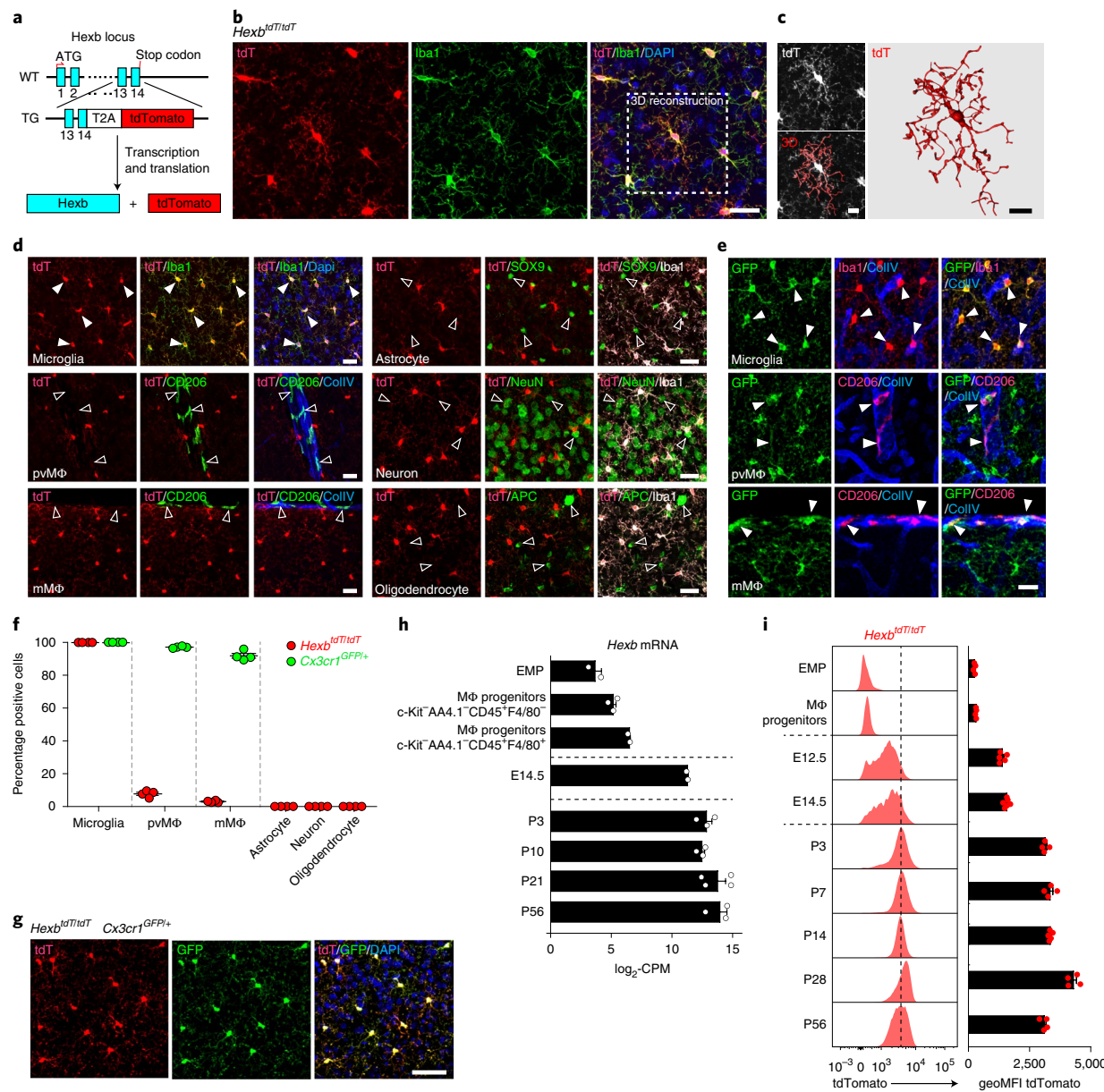


Fig. 3 | Generation and characterization of Hexb^{tdTomato} mice. **a**, Schematic overview of gene targeting. CRISPR/Cas9-mediated knockin of the T2A-tdTomato cassette into the Hexb locus. The T2A-tdTomato cassette was inserted immediately upstream of the Hexb stop codon after exon 14. Following transcription and translation, a T2A-mediated self-cleavage takes place, which allows both Hexb and tdT protein expression under the control of the endogenous Hexb gene locus. **b**, Representative immunofluorescence images for tdT (red) and ionized calcium binding adaptor molecule (Iba1) (green) to visualize microglia and for DAPI (blue) to stain nuclei from the cortex of 8-week-old Hexb^{tdT/tdT} mice. Scale bar, 25 μ m. Representative pictures out of four investigated mice are shown. **c**, Three-dimensionally (3D) reconstructed images of dashed frame shown in **b**, depicting single tdT-expressing microglia with fine processes in the brains of Hexb^{tdT/tdT} mice. Scale bar, 10 μ m. **d**, Direct fluorescence microscopic visualization revealed tdT⁺ ramified cells with typical microglial morphology in the brains of 8-week-old Hexb^{tdT/tdT} mice. Iba1-immunoreactivity is shown for parenchymal microglia (green or white), CD206 for CAMs, including perivascular (pVMP, green) and meningeal (mMΦ, green) macrophages, SOX9 for astrocytes (green), NeuN for neurons (green), APC for oligodendrocytes (green) and collagen IV for basement membranes (Col IV, blue), respectively. White and blank arrowheads indicate either tdT⁺ or tdT⁻ cells, respectively. Scale bars, 25 μ m. Representative pictures out of four investigated mice are shown. **e**, Representative immunofluorescence images depicting GFP signals in the brains of 8-week-old Cx3cr1^{GFP/+} mice. Immunolabeling was performed for Iba1 (red), CD206 for CAMs including pVMP and mMΦ (red) and collagen IV for basement membranes (Col IV, blue), respectively. White arrowheads indicate GFP⁺ cells. Scale bars, 20 μ m. Representative pictures out of four investigated mice are shown. **f**, Quantification of tdT⁺ or GFP⁺ microglia, pVMP, mMΦ, astrocytes, neurons and oligodendrocytes in the CNS of Hexb^{tdT/tdT} or Cx3cr1^{GFP/+} mice based on immunofluorescence-based evaluations. Each symbol represents one individual animal. Means \pm s.e.m. are shown from four animals. **g**, Typical confocal immunofluorescence pictures showing colocalization of tdT and GFP signals in the brains of 8-week-old double transgenic Hexb^{tdT/tdT}Cx3cr1^{GFP/+} mice. Scale bars, 50 μ m. Representative pictures out of four investigated mice are shown. **h**, Expression of Hexb transcripts in yolk sac progenitors (erythromyeloid progenitors (EMPs), macrophage (MΦ) progenitors and microglia sorted by FACS during embryonic (E) or postnatal (P) development). Each symbol represents one individual animal (EMPs, n=2; MΦ progenitors (c-Kit⁻AA4.1⁻CD45⁻F4/80⁻), n=3; MΦ progenitors (c-Kit⁻AA4.1⁻CD45⁻F4/80⁺), n=2; E14.5, n=2; P3, n=3; P10, n=3; P21, n=4; P56, n=3). Bars represent means \pm s.e.m. CPM, counts per million. **i**, Flow cytometry-based measurement of tdT in c-Kit⁺AA4.1⁺CD45⁻ EMPs, c-Kit⁻AA4.1⁻CD45⁻ MΦ progenitors, CD45^{lo}CD11b⁺ microglia in Hexb^{tdT/tdT} mice during development. Each symbol represents one individual animal (EMPs, n=4; MΦ progenitors, n=4; E12.5, n=5; E14.5, n=6; P3, n=4; P7, n=4; P14, n=5; P28, n=4; P56, n=4). Bars represent means \pm s.e.m.

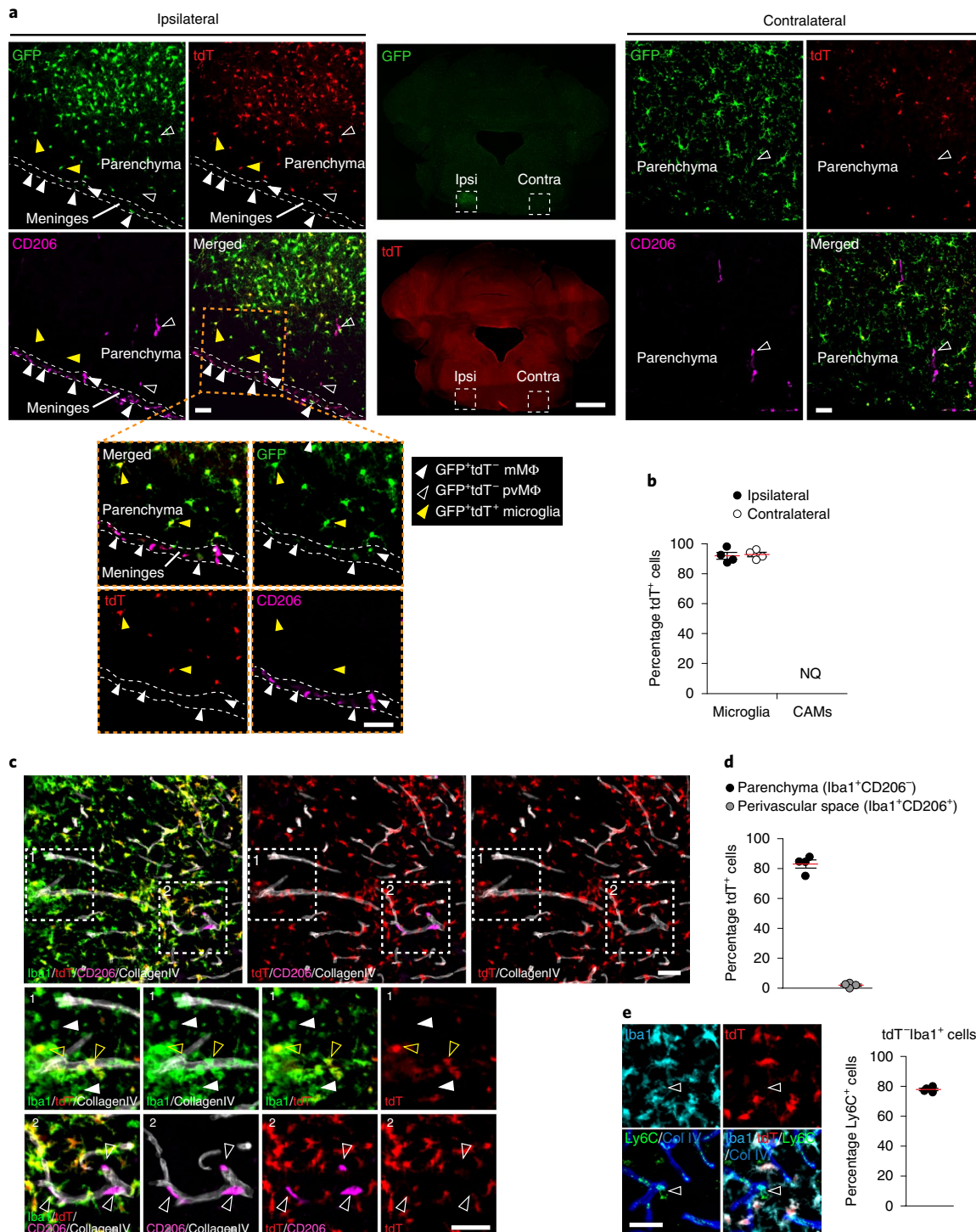


Fig. 4 | Continuous detection of *Hexb^{tdT}* microglia during neurodegeneration and autoimmune demyelination. **a**, Representative immunofluorescence images for GFP (green), tdT (red) and CD206 (purple) of the facial nucleus of *Hexb^{tdT/+}Cx3cr1^{GFP/+}* 7 d after FNX depicting lesioned ipsilateral (left) or contralateral control side (right) or overview (FNX, middle). Parenchymal microglia express both GFP and tdT (filled yellow triangles), whereas mMΦ and pvMΦ are positive for GFP only (filled white triangles or open triangles). Zoom is shown below. Scale bars, 1,000 μm (overview), 50 μm (detailed images) and 50 μm (zoom images). Representative pictures out of four investigated mice are shown. **b**, Quantification thereof. Each symbol represents an individual mouse. Means ± s.e.m. are shown from four animals. NQ, not quantifiable. **c**, Direct fluorescence microscopic visualization revealed tdT⁺ (red) Iba1⁺ (green) CD206⁻ (pink) microglia and tdT⁺ Iba1⁺ CD206⁺ (purple) pvMΦ at peak phase during autoimmune inflammation (EAE) in *Hexb^{tdT/+}* mice. Inset 1 (dashed frame) indicates a core affected site that includes tdT⁺ Iba1⁺ branched cells (yellow arrowheads) and tdT⁺ Iba1⁺ round-shape cells (filled white arrowheads). Inset 2 (dashed frame) illustrates tdT⁺ Iba1⁺ CD206⁺ pvMΦ (white arrowheads). Scale bars, 50 μm (overview), 50 μm (inset). Representative pictures out of four investigated mice are shown. **d**, Quantification of tdT-expressing cells in the parenchyma and the perivascular space during EAE. Each symbol represents an individual mouse. Means ± s.e.m. are shown from four animals. **e**, Left, representative images showing Iba1⁺ (light blue), tdT⁺ (red) and Ly6C⁺ (green) cell (white arrowheads) at peak phase during autoimmune inflammation (EAE) in *Hexb^{tdT/+}* mice. Scale bars, 50 μm. Right, quantification of Iba1⁺ tdT⁺ Ly6C⁺ cells. Means ± s.e.m. are shown from four animals.

perivascular Iba1⁺CD206⁺ cells did not express tdT (Fig. 4c,d). However, tdT⁻ Iba1⁺CD206⁺ cells were also detected in the inflamed CNS, most of which expressed a monocyte marker Ly6C (Fig. 4e), presumably representing infiltrating myeloid cells. Despite the fact that we cannot formally exclude the possibility that infiltrating myeloid cells could start to express *Hexb* in the CNS parenchyma, these data strongly indicate that *Hexb*^{tdT} mice are a valuable tool to study microglia responses to disease *in vivo*.

We next tested the suitability of the tdT signal for intravital multiphoton imaging via a cranial window to capture microglia responses on laser lesioning *in vivo* over 30–120 min (Fig. 5a–e). Comparison of the motility of microglial processes from *Cx3cr1*^{GFP/+} mice with those of microglia from *Hexb*^{tdT/tdT} animals did not show overt differences during steady-state conditions or after laser lesion, indicating that tdT labeling under the control of the *Hexb* gene locus does not alter microglia surveillance function and reactive behavior (Fig. 5d,e), and can therefore be used for investigations of microglial dynamics even in the deeper layer (at least 500 μm from the surface of the brain; Fig. 5c) *in vivo*.

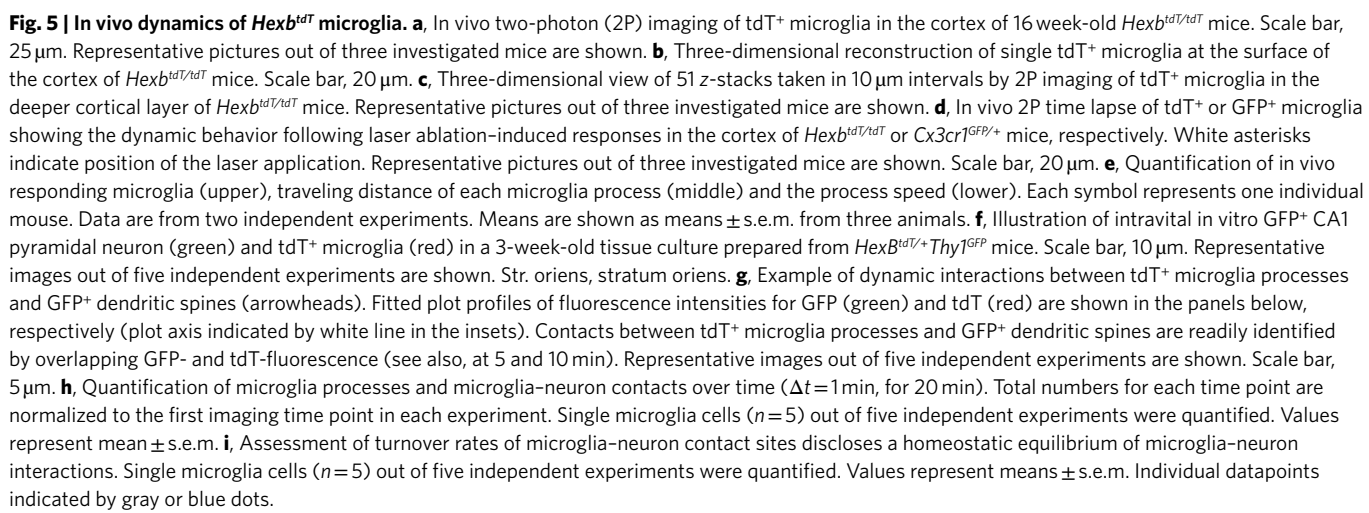
Emerging research has implicated microglia in brain wiring in the healthy brain²⁷. During development, complement factors localize to synapses and mediate synapse elimination by phagocytic microglia²⁸. To determine whether microglial interactions with synapses can be examined in our system, we used high-resolution confocal live-cell imaging of organotypic entorhino-hippocampal tissues from *Hexb*^{tdT/+}*Thy1*^{GFP/+} mice (Fig. 5f). Contacts between tdT⁺ microglia processes and GFP⁺ dendritic spines were readily identified using quantitative measurements of fluorescence intensities (Fig. 5g). Time-lapse imaging experiments of up to 20 min showed that tdT⁺ microglia processes were very motile, continuously interacting with GFP⁺ dendrites, and undergoing cycles of de novo extension and withdrawal, while maintaining total numbers of processes and contact sites in steady state (Fig. 5h,i). Overall, the *Hexb*^{tdT} line represents a versatile tool to follow microglia behavior *in vivo* over a prolonged time period and even during disease conditions.

Establishment of an inducible *Hexb*^{CreERT2} system to investigate microglial function. To exploit *Hexb* promoter activity for fate mapping and gene deletion, we inserted a T2A-CreERT2 cassette into the *Hexb* locus just before the stop codon (*Hexb*^{CreERT2}) (Fig. 6a). In this condition, the Cre recombinase is expressed in a *Hexb*-specific manner and requires the presence of the estrogen antagonist TAM for activation. Given the restricted expression of *Hexb* on CNS microglia but barely on CAMs, *Hexb*^{CreERT2} mice should be particularly valuable for studying microglial functions

in vivo. To probe this potential, we compared these mice with existing models used for microglia targeting, namely mice expressing Cre recombinase from the *Sall1* locus (*Sall1*^{CreERT2})^{29,30} and the *Cx3cr1* locus (*Cx3cr1*^{CreERT2})^{17,18} with respect to their microglial reporter gene activation pattern (Fig. 6 and Supplementary Fig. 7). To this end, all three lines were crossed to ROSA26(R26)-YFP reporter animals and the respective offspring were challenged with TAM at postnatal days P1 and P3 and subsequently analyzed during adulthood at P42 (Fig. 6b). This approach takes advantage of the unique features of microglia of homeostatic proliferation without any input from circulating blood cells whereas short-lived blood cells, derived from the definitive hematopoiesis such as monocytes, will be replaced after few days¹⁸.

We started by exploring the recombination efficacy in the CNS and peripheral blood (Supplementary Fig. 7a–d). Microglia and CAMs were isolated from the brains of adult mice and analyzed by flow cytometry for the percentage of YFP⁺ cells. In *Hexb*^{CreERT2/CreERT2}*R26*^{yfp/yfp} mice, most microglial cells but not CAMs, CD45⁻CD11b⁻ CNS cells or circulating Ly6C^{hi}, Ly6C^{lo} monocytes or Ly6G⁺ granulocytes expressed yellow fluorescent protein (YFP) at 6 weeks after TAM treatment. In contrast, *Cx3cr1*^{CreERT2/+}*R26*^{yfp/yfp} mice revealed high recombination rates in both microglia and CAMs but no other CNS or peripheral cells as reported earlier¹⁰. *Sall1*^{CreERT2/+}*R26*^{yfp/yfp} mice showed no YFP labeling of CAMs but recombination in CD45⁻CD11b⁻ CNS cells (18.5 ± 2.9% YFP⁺ cells), suggesting ectopic recombination in the nonhematopoietic compartment as recently reported³¹.

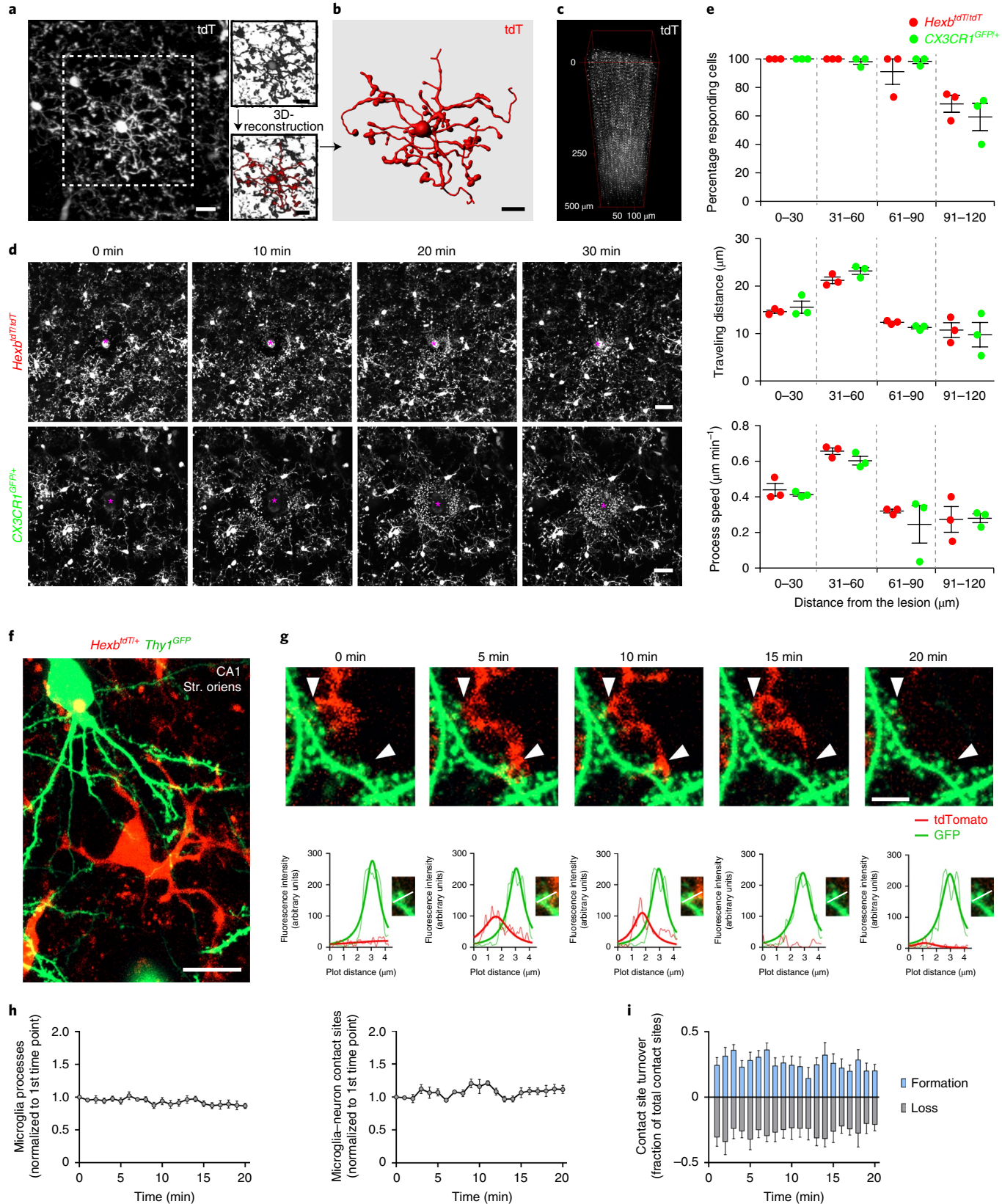
To further corroborate these findings *in situ*, we thoroughly examined the CNS tissues of all three mouse lines (Fig. 6c–f). Histological examination of TAM-treated *Hexb*^{CreERT2/CreERT2}*R26*^{yfp/yfp} mice confirmed the FACS data and revealed a high percentage of Iba1-labeled cortical microglia that coexpressed YFP (90.8 ± 1.6%), whereas pMΦ (6.8 ± 1.6%), mMΦ (0.4 ± 0.1%) showed barely any signs of recombination. No signs of recombination were observed in astrocytes, neurons and oligodendrocytes (Fig. 6c,f and Supplementary Fig. 8). Likewise, the TAM treatment at later perinatal time points (P7 and P9) also induced YFP expression in microglia at a very high level (93.2 ± 2.1%, Fig. 6b,f). In contrast, F4/80⁺ tissue macrophages in the kidney, spleen and liver were virtually not labeled with YFP in *Hexb*^{CreERT2/CreERT2}*R26*^{yfp/yfp} mice (Supplementary Fig. 9). High YFP expression in microglia was also detected in the brains of *Cx3cr1*^{CreERT2/+}*R26*^{yfp/yfp} mice accompanied by additional high recombination rates in pMΦ (95.3 ± 0.5%) and mMΦ (90.9 ± 2.0%), corresponding to the reported *Cx3cr1* expression in CAMs¹⁰ (Fig. 6d,f). We observed no ectopic YFP expression in astrocytes, neurons or oligodendrocytes in this line.



Notably, *Sall1*^{CreERT2/+}*R26*^{yfp/yfp} mice revealed high levels YFP expression in microglia but not pvMΦ and mMΦ, and surprisingly high rates of YFP expression in Sox9⁺ astrocytes (68.2 ± 2.0%) and APC⁺ oligodendrocytes (34.9 ± 1.5%) (Fig. 6e,f), suggesting ectopic gene

recombination and confirming the FACS results (Supplementary Fig. 7c).

Taken together, the newly developed TAM-inducible *Hexb*^{CreERT2} line provides a valuable tool to efficiently target microglia with high



frequency and stable genetic modification over a prolonged period of time by only marginally affecting CAMs.

Hexb^{CreERT2}-based fate mapping reveals cell-autonomous progenitors for repopulating microglia. Microglial repopulation biology has been investigated extensively in several recent studies using either genetically mediated³² or pharmacological approaches³³. The latter technique used several potent colony stimulating factor-1 receptor (CSF1R) inhibitors such as BLZ945, which efficiently depletes microglia^{9,33} and CAMs¹¹. Usage of this chemical compound has recently uncovered that remaining and surviving endogenous microglia act as the source for subsequent repopulation of the microglial network following depletion^{34,35}. However, whether repopulated microglia and CAMs share a common myeloid progenitor or have distinct cell-autonomous sources remains unknown.

We therefore depleted all CSF1R-dependent CNS macrophages in adult *Hexb^{CreERT2/CreERT2}R26^{yfp/yfp}* mice using BLZ945 and performed fate mapping experiments to study their repopulation kinetics (Fig. 7a). Oral treatment of vehicle or BLZ945 was performed for 1 week and repopulation was afterward assessed 2 weeks later. Immunohistochemical analysis confirmed that 1 d after the last treatment, cortical microglia as well as pvMΦ and mMΦ were efficiently depleted (Fig. 7b,c). Two weeks after the end of BLZ945 treatment, microglia and pvMΦ, mMΦ cell numbers were restored. Repopulated Iba1⁺ microglia still exhibited high indicator gene labeling, whereas reestablished populations of pvMΦ, mMΦ revealed only borderline YFP expression as seen before treatment (Fig. 7d), indicating CAM-specific progenitors that are different from those from microglia.

Taken together, these data provide clear evidence that during steady state in adulthood the different macrophage entities in the CNS, namely microglia and border-associated CAMs, exist independently from each other without any cellular exchanges and that during depletion-induced repopulation compartment- and niche-specific surviving myeloid cells exist that mediate the replenishment.

The new inducible *Hexb^{CreERT2}* system allows the investigation of microglial function during adulthood. To further assess the use of the *Hexb^{CreERT2}* mouse line for studying microglial functions in adulthood, we next examined the recombination efficiency as well as the kinetics of gene recombination by histology and FACS analysis in adult *Hexb^{CreERT2/CreERT2}R26^{tdT/tdT}* and *Hexb^{CreERT2/CreERT2}R26^{yfp/yfp}* mice compared to *Cx3cr1^{CreERT2/+}R26^{yfp/yfp}*, *Cx3cr1^{CreERT2/+}R26^{tdT/tdT}* and *Sall1^{CreERT2/+}R26^{yfp/yfp}* mice at 1 or 4 weeks after TAM injection (Supplementary Figs. 10 and 11). A similar pattern of reporter expression was observed in adult *Hexb^{CreERT2/CreERT2}R26^{yfp/yfp}* mice when

compared to early postnatal TAM treatment. However, reporter gene activation in microglia from adult *Hexb^{CreERT2/CreERT2}R26^{yfp/yfp}* animals was reduced (Supplementary Fig. 10). Notably, microglial labeling in *Hexb^{CreERT2/CreERT2}R26^{tdT/tdT}* animals was higher when compared to *Hexb^{CreERT2/CreERT2}R26^{yfp/yfp}* mice that is potentially due to distinct rearrangement frequencies associated with the reporter lines as described recently³⁶.

Analysis of mice 4 weeks post TAM confirmed persistent YFP labeling of microglia and confirmed the earlier notion of a stable population^{37,38}, whereas labeling of Ly6C^{hi}, Ly6C^{lo} monocytes and Ly6G⁺ granulocytes from *Hexb^{CreERT2/CreERT2}R26^{tdT/tdT}* animals disappeared (Supplementary Fig. 11) because of their swift replacement with nonrecombined bone marrow-derived cells.

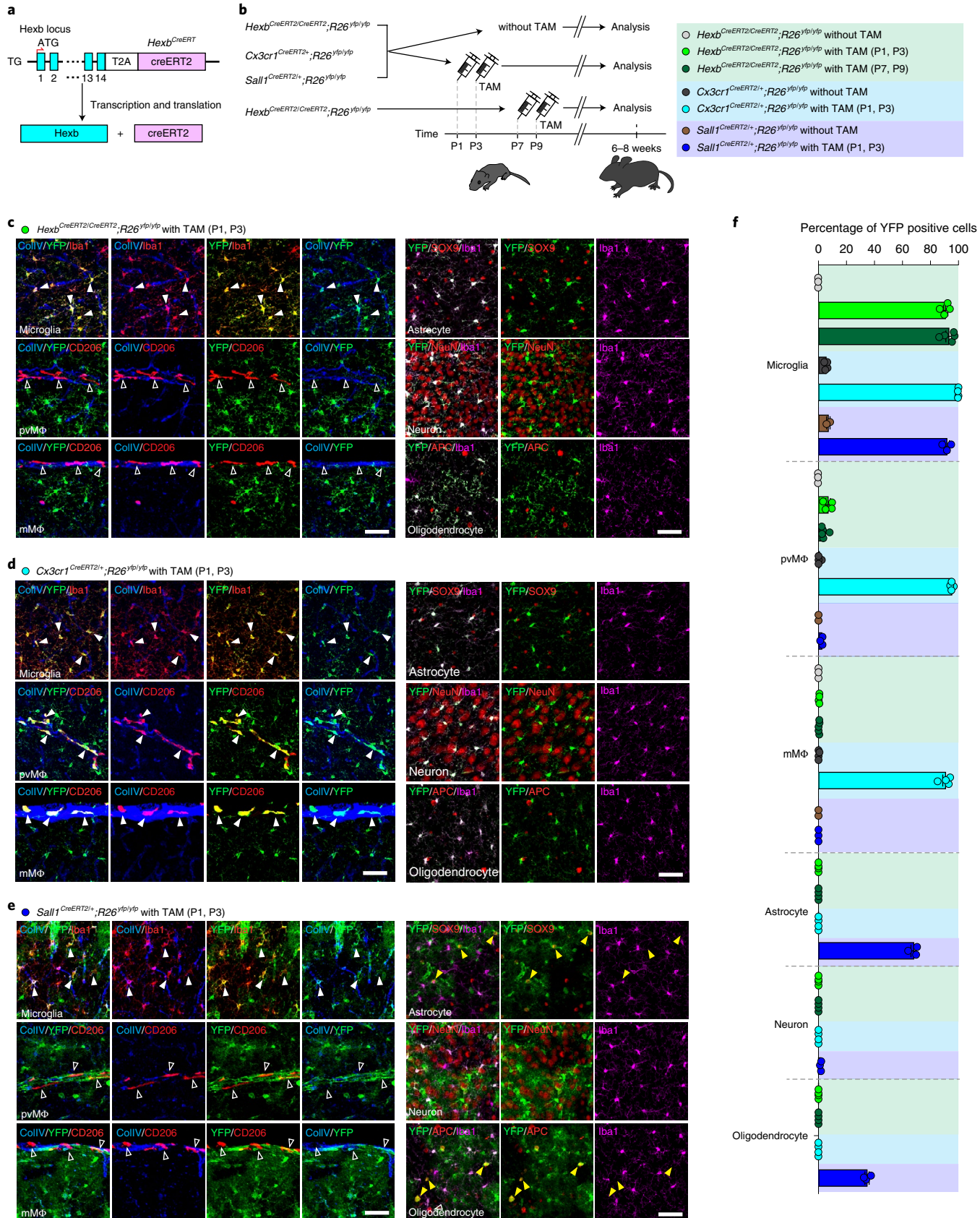
To boost the recombination efficiency in adult *Hexb^{CreERT2}* mice, we established an optimized TAM protocol (Supplementary Fig. 12a), which induced YFP expression in microglia at a high level with some variation across the CNS (olfactory bulb: $89.1 \pm 1.1\%$, cortex: $80.5 \pm 1.2\%$, hippocampus: $83.3 \pm 0.6\%$, cerebellum: $78.8 \pm 1.0\%$ and spinal cord: $70.7 \pm 1.1\%$) (Supplementary Fig. 12c,d), but much less in pvMΦ ($1.5 \pm 0.5\%$) and mMΦ ($0.2 \pm 0.1\%$). YFP⁺ blood cells in *Hexb^{CreERT2}* mice were again replaced by nonrecombined cells by 28 d after TAM treatment (Supplementary Fig. 12b). In the periphery of *Hexb^{CreERT2/CreERT2}R26^{yfp/yfp}* mice, F4/80⁺ tissue-resident macrophages in the kidney, but not spleen and liver, were found to be YFP⁺ (Supplementary Fig. 13a–c).

Selective effects on microglia in *Hexb^{CreERT2/CreERT2}Csf1r^{fl/fl}* mice. To test the functionality of the new microglia-restricted inducible *Hexb^{CreERT2}* line, we generated *Hexb^{CreERT2/CreERT2}Csf1r^{fl/fl}* mice (Fig. 8a). CSF1R engagement is an essential survival signal for all CNS macrophages and therefore, microglia and CAMs are absent in CSF1R-deficient mice³⁹. We administered TAM to adult *Hexb^{CreERT2/CreERT2}Csf1r^{fl/fl}* and *Hexb^{CreERT2/CreERT2}Csf1r^{+/+}* control mice and subsequently analyzed the animals 3 d after the last TAM injection. Brains of treated mice showed no overt abnormalities. However, FACS analysis of *Hexb^{CreERT2/CreERT2}Csf1r^{fl/fl}* mice revealed significantly ($P = 0.0051$) lower CD115 (CSF1R) levels on the surface of microglia, whereas expression levels were unchanged on CAMs (Fig. 8b,c). To further investigate the consequences of CSF1R deletion specifically on microglia, we performed a detailed neuropathological analysis of the brain tissues (Fig. 8d–g). In TAM-treated *Hexb^{CreERT2/CreERT2}Csf1r^{+/+}* mice, we detected 227.4 ± 6.0 Iba1⁺ microglia per mm² with typical surveilling morphology such as round to spindle-shaped somata and a distinct arborization pattern with finely delineated processes (Fig. 8d,e). In contrast, microglia numbers from TAM-treated *Hexb^{CreERT2/CreERT2}Csf1r^{fl/fl}* mice were significantly ($P < 0.0001$) reduced in number to

Fig. 6 | Generation and comparative analysis of *Hexb^{CreERT2}* mice. **a**, Targeting scheme. The T2A-CreERT2 cassette was knocked into the *Hexb* locus just before the stop codon. From the resulting polycistronic RNA, a fusion protein is translated, which, due to the activity of the self-cleaving T2A peptide, gives rise to *Hexb* and the CreERT protein. TG, transgene. **b**, Scheme for the induction of recombination (injection of TAM) and subsequent analysis in *Hexb^{CreERT2/CreERT2}R26^{yfp/yfp}*, *Cx3cr1^{CreERT2/+}R26^{yfp/yfp}* and *Sall1^{CreERT2/+}R26^{yfp/yfp}* mice, respectively. **c**, Direct fluorescence microscopic visualization reveals YFP signals in Iba1⁺ microglia (red) but not in pvMΦ (CD206, red), mMΦ (CD206, red), astrocytes (SOX9, red), neurons (NeuN, red) or oligodendrocyte (APC, red) in the cortex of adult *Hexb^{CreERT2/CreERT2}R26^{yfp/yfp}* mice. Collagen IV is shown in blue. Filled triangles indicate double positive microglia, empty triangles show single positive pvMΦ and mMΦ. Scale bars, 50 μm. Representative images from four mice are shown. **d**, Representative immunofluorescence images showing YFP labeling within microglia (Iba1, red) but not pvMΦ, mMΦ (both CD206, red), astrocytes (SOX9, red), neurons (NeuN, red) and oligodendrocytes (APC, red) in the cortex of adult *Cx3cr1^{CreERT2/+}R26^{yfp/yfp}* mice. Filled triangles indicate double positive microglia, pvMΦ and mMΦ. Scale bars, 50 μm. Representative images from five mice are shown. **e**, Typical immunofluorescence images showing YFP labeling within microglia (Iba1, red) but not pvMΦ, mMΦ (both CD206, red), astrocytes (SOX9, red), neurons (NeuN, red) and oligodendrocytes (APC, red) in the cortex of adult *Sall1^{CreERT2/+}R26^{yfp/yfp}* mice. Filled white triangles indicate double positive microglia. Empty triangles show single positive pvMΦ and mMΦ. Filled yellow triangles indicate double positive astrocytes and oligodendrocytes. Scale bars, 50 μm. Representative images from five mice are shown. **f**, Quantification of recombination efficacy in several CNS cells of *Hexb^{CreERT2/CreERT2}R26^{yfp/yfp}*, *Cx3cr1^{CreERT2/+}R26^{yfp/yfp}* and *Sall1^{CreERT2/+}R26^{yfp/yfp}* mice, respectively. Each symbol represents one mouse (*Hexb^{CreERT2/CreERT2}R26^{yfp/yfp}* without TAM, $n=3$; *Hexb^{CreERT2/CreERT2}R26^{yfp/yfp}* with TAM (P1, P3), $n=4$; *Hexb^{CreERT2/CreERT2}R26^{yfp/yfp}* with TAM (P7, P9), $n=5$; *Cx3cr1^{CreERT2/+}R26^{yfp/yfp}* without TAM, $n=4$; *Cx3cr1^{CreERT2/+}R26^{yfp/yfp}* with TAM (P1, P3), $n=4$; *Sall1^{CreERT2/+}R26^{yfp/yfp}* without TAM, $n=2$; *Sall1^{CreERT2/+}R26^{yfp/yfp}* with TAM (P1, P3), $n=3$). Three sections per mouse were quantified (means \pm s.e.m.).

138.6 ± 4.3 Iba1⁺ cells per mm² without obvious alterations in morphology (Fig. 8d,e). A similar reduction in the number of microglia was observed in the spinal cord of *Hexb*^{CreERT2/CreERT2}

Csf1r^{f/f} mice (Supplementary Fig. 14). In contrast, numbers of CD206⁺ pvMΦ and mMΦ did not differ between TAM-treated *Hexb*^{CreERT2/CreERT2}*Csf1r*^{f/f} (pvMΦ, 10.6 ± 0.4 cells per mm²; mMΦ,



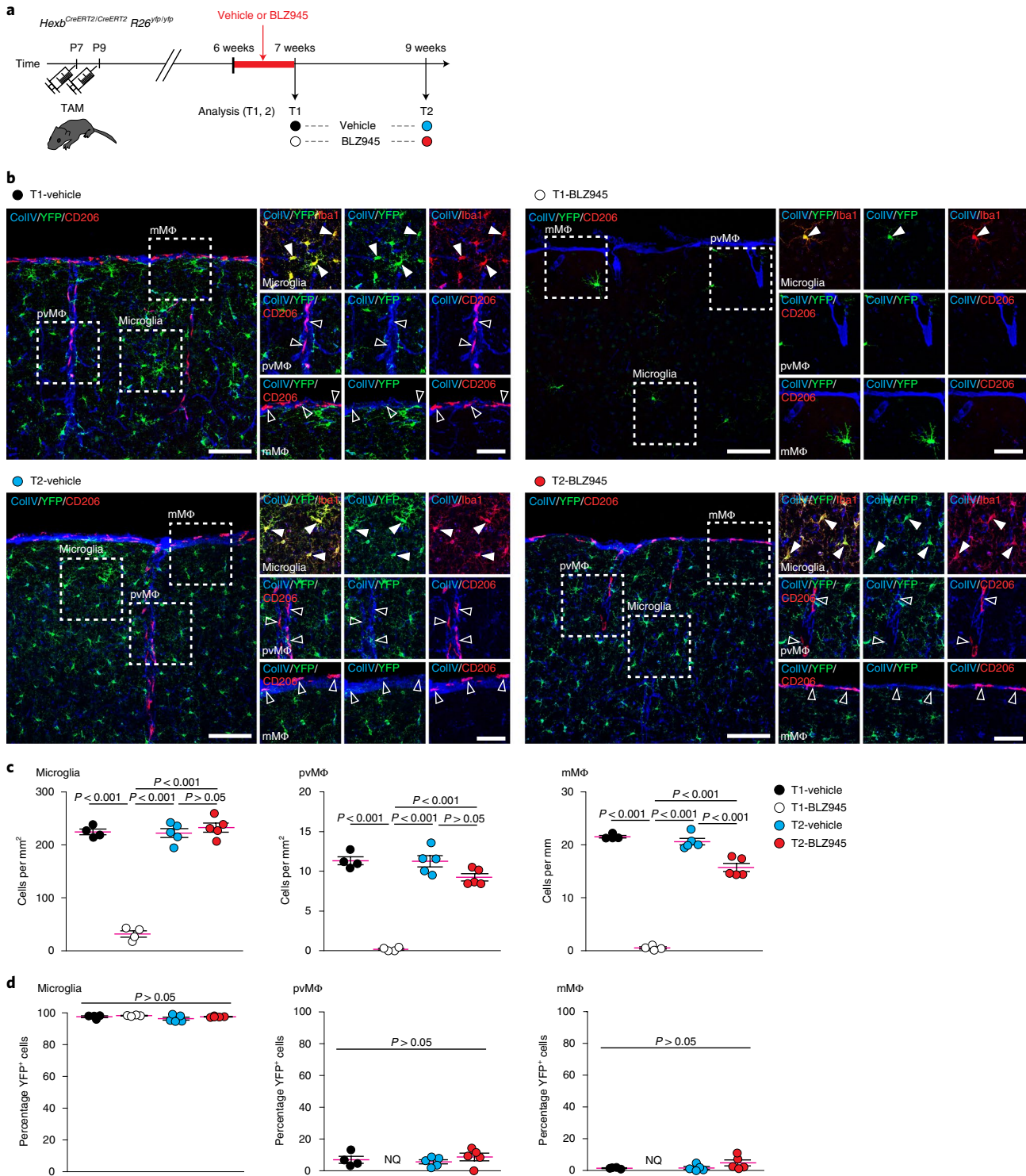


Fig. 7 | Fate mapping following CNS macrophage depletion using *Hexb*^{CreERT2/CreERT2} *R26*^{Yfp/Yfp} mice. **a**, Scheme of experimental setup. Adult *Hexb*^{CreERT2/CreERT2} *R26*^{Yfp/Yfp} mice were injected with TAM at postnatal day 7 (P7) and P9 and subsequently daily treated with BLZ945 or vehicle at the age of 6 weeks for 7 d. Analysis was then performed 2 weeks after the treatment. Colored circles correspond to the different time points and are shown again in the immunofluorescence pictures in **b**. **b**, Representative immunofluorescence images of microglia (Iba1), pvMΦ and mMΦ (both CD206) images from vehicle- or BLZ945-treated *Hexb*^{CreERT2/CreERT2} *R26*^{Yfp/Yfp} mice at the time points visualized in **a**. Filled triangles indicate Iba1⁺YFP⁺ microglia, and blank white triangles indicate YFP⁻ microglia, pvMΦ and mMΦ, respectively. Representative images from four mice (T1 analysis) or five mice (T2) are depicted. Scale bars, 100 μm (large image) and 50 μm (dashed frame). **c**, Quantification of microglia (Iba1), pvMΦ and mMΦ (both CD206) in naive and BLZ945- or vehicle-treated mice at different time points. Each symbol represents one mouse (T1-vehicle, $n=4$; T1-BLZ945, $n=4$; T2-vehicle, $n=5$ and T2-BLZ945, $n=5$). Three sections per mouse were quantified (means \pm s.e.m.). One-way ANOVA with post hoc Tukey's multiple comparisons test was used for statistical analysis. **d**, Percentages of YFP-labeled microglia (Iba1), pvMΦ and mMΦ (both CD206) during depletion and repopulation. Three sections per mouse were quantified (T1-vehicle, $n=4$; T1-BLZ945, $n=4$; T2-vehicle, $n=5$ and T2-BLZ945, $n=5$). Values represent means \pm s.e.m. One-way ANOVA with post hoc Tukey's multiple comparisons test was used for statistical analysis.

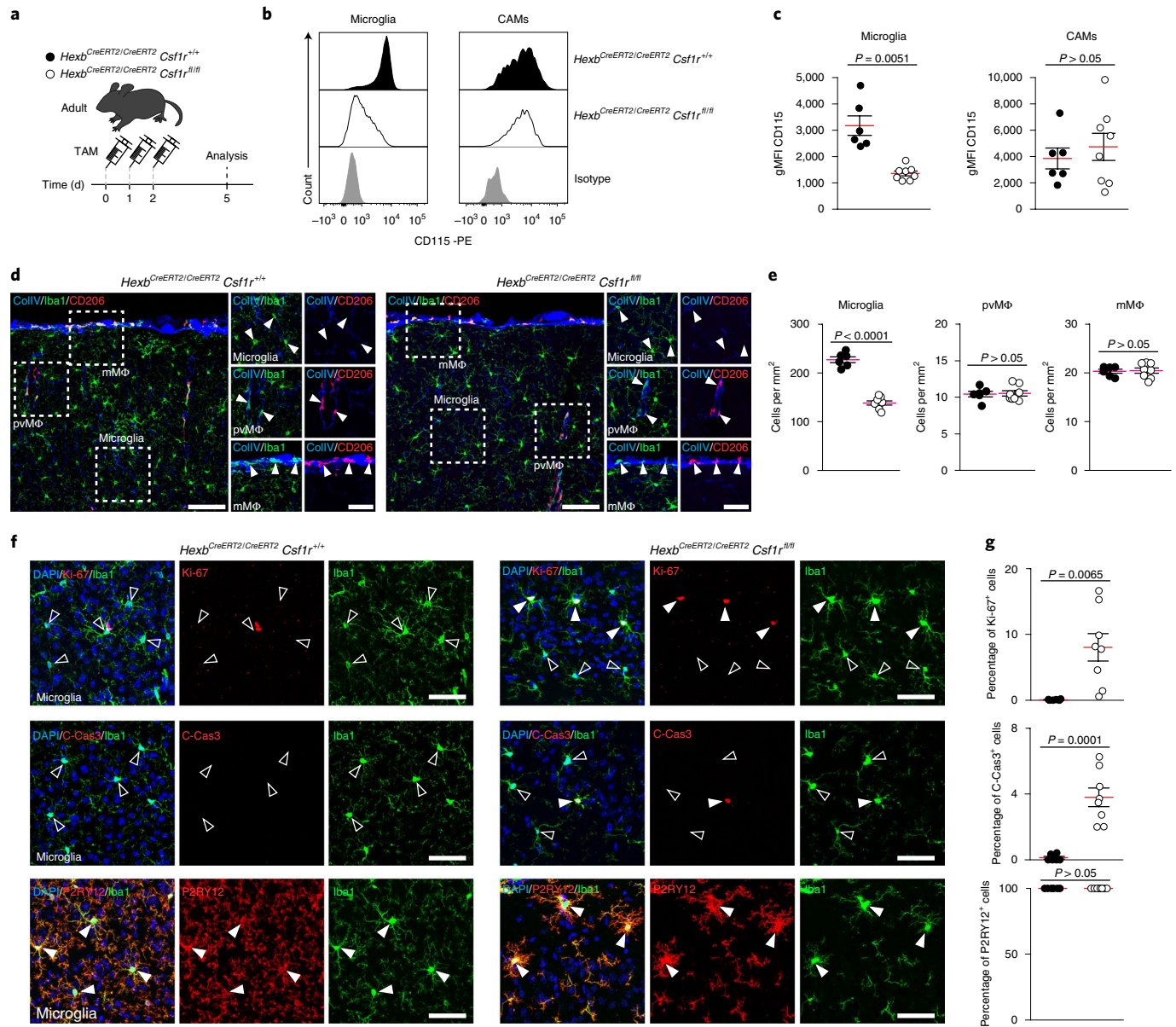


Fig. 8 | Effects of *Csf1r* deletion on microglia but not CAMs. **a**, Scheme for experimental setup. Adult *Hexb*^{CreERT2/CreERT2} *Csf1r*^{+/+} and *Hexb*^{CreERT2/CreERT2} *Csf1r*^{f/f} mice were injected with TAM three times (days 0–2) and were subsequently analyzed at day 5. **b**, Surface expression of CD115 (*Csf1r*) measured by flow cytometry at day 5. Representative histograms showing CD115 expression on microglia (left) and CAMs (right) from *Hexb*^{CreERT2/CreERT2} *Csf1r*^{+/+} (filled histogram) and *Hexb*^{CreERT2/CreERT2} *Csf1r*^{f/f} (open histogram) mice. Isotype controls are shown in gray. Representative plots out of six (*Hexb*^{CreERT2/CreERT2} *Csf1r*^{+/+}) or eight mice (*Hexb*^{CreERT2/CreERT2} *Csf1r*^{f/f}) used are shown. **c**, Quantification thereof. Each symbol represents one mouse (*Hexb*^{CreERT2/CreERT2} *Csf1r*^{+/+}, *n* = 6; *Hexb*^{CreERT2/CreERT2} *Csf1r*^{f/f}, *n* = 8). Means \pm s.e.m. are shown. Student's *t*-test was used for statistics. **d**, Representative immunofluorescence images showing microglia (Iba1, green) and mMΦ (CD206, red) in the cortex of *Hexb*^{CreERT2/CreERT2} *Csf1r*^{f/f} mice compared to *Hexb*^{CreERT2/CreERT2} *Csf1r*^{+/+} controls. Filled triangles indicate Iba1⁺ microglia or CD206⁺ pMΦ and mMΦ. Scale bars, 100 μ m (large image) and 50 μ m (dashed frame). Representative images from four (*Hexb*^{CreERT2/CreERT2} *Csf1r*^{+/+}) or five mice (*Hexb*^{CreERT2/CreERT2} *Csf1r*^{f/f}) are shown. **e**, Quantification thereof. Each symbol represents one mouse (*Hexb*^{CreERT2/CreERT2} *Csf1r*^{+/+}, *n* = 6; *Hexb*^{CreERT2/CreERT2} *Csf1r*^{f/f}, *n* = 8). Three sections per mouse were quantified (means \pm s.e.m.). Student's *t*-test was used. **f**, Typical immunofluorescence pictures for microglia (Iba1, green), DAPI (blue), Ki-67 (red), cleaved caspase 3 (C-Cas3, red) and P2RY12 (red) in the cortex of *Hexb*^{CreERT2/CreERT2} *Csf1r*^{f/f} mice and *Hexb*^{CreERT2/CreERT2} *Csf1r*^{+/+} mice. Filled triangles indicate double positive cells, open triangles point to single labeled cells. Scale bars, 50 μ m. Representative images from six (*Hexb*^{CreERT2/CreERT2} *Csf1r*^{+/+}) or eight mice (*Hexb*^{CreERT2/CreERT2} *Csf1r*^{f/f}) are shown. **g**, Quantitative results of immunofluorescence images. Each symbol represents one mouse (*Hexb*^{CreERT2/CreERT2} *Csf1r*^{+/+}, *n* = 6; *Hexb*^{CreERT2/CreERT2} *Csf1r*^{f/f}, *n* = 8). Three sections per mouse were quantified (means \pm s.e.m.). Student's *t*-test was used for statistical analysis.

20.5 \pm 0.5 cells per mm²) and *Hexb*^{CreERT2/CreERT2} *Csf1r*^{+/+} mice (pMΦ, 10.5 \pm 0.4 cells per mm²; mMΦ, 20.4 \pm 0.4 cells per mm²) (Fig. 8d,e). Likewise, the number of F4/80⁺ macrophages in the kidney was also reduced in *Hexb*^{CreERT2/CreERT2} *Csf1r*^{f/f} mice (Supplementary Fig. 13d–f).

To get more insights into the functional consequences of CSF1R deficiency selectively on microglia, we performed further analysis and detected higher proliferation rates and an increased number of apoptotic microglia in *Hexb*^{CreERT2/CreERT2} *Csf1r*^{f/f} mice compared to controls (Fig. 8f,g). This indicates that the impaired microglial

survival is partially compensated by proliferative expansion. On the other hand, remaining microglia in *Hexb*^{CreERT2/CreERT2}*Csf1r*^{f/f} mice still expressed the surface marker P2RY12 at a level comparable to *Hexb*^{CreERT2/CreERT2}*Csf1r*^{r/+} controls (Fig. 8f,g).

These results indicate that microglia-specific CSF1R expression (modulated by our new *Hexb*^{CreERT2} system) represents a valuable tool to analyze the survival of parenchymal macrophages in the CNS without affecting the macrophage populations at CNS interfaces.

Discussion

We report transgenic mouse models for highly enriched microglia gene targeting with only minimal effects on CAMs in homeostasis and in several models of neuroinflammatory and neurodegenerative diseases. By using large-scale single-cell RNA-sequencing, we were first able to monitor the expression of microglia core genes under pathological conditions. The expression of most of the examined well-known microglia-related genes, such as *P2ry12*, *Tmem119*, *Gpr34*, *Tgfb1*, *Fcrls*, *Siglech*, *Slc2a5* and *Sall1*, was substantially reduced with perturbations or generally too low to use them for microglia gene targeting under disease conditions *in vivo*. We confirmed the specificity of *P2ry12* expression for microglia as described before for the healthy CNS³¹. On activation, however, *P2ry12* expression was downregulated, which is in line with the findings made from neuroinflammation in patients with multiple sclerosis and in animal models of the disease^{40,41}. Our data expand these findings by showing that this prototypical microglial gene is strongly reduced; not only during EAE, but also in the two tested neurodegeneration models, FNX and the 5xFAD model of Alzheimer's disease. Transmembrane protein 119 (*Tmem119*), a cell-surface protein of unknown function, was also recently identified as a highly expressed microglia-specific marker in both mice and humans⁴² that is clearly absent in CAMs¹⁰. Here, we show that *Tmem119* was among the most strongly downregulated genes with almost absent expression during cuprizone-induced demyelination, EAE, and in the 5xFAD model of Alzheimer's disease. Furthermore, a very recent targeting approach using the *Tmem119* locus in mice revealed ectopic expression of *Tmem119* in CD34⁺ vessels in the CNS as well as in pial cells inside the leptomeninges⁴³.

In contrast, we found that *Hexb* was persistently expressed by microglia and much less by CAMs in various disease models. The *Hexb* gene encodes the beta subunit of hexosaminidase B, which is the lysosomal enzyme required for the degradation of the ganglioside GM2. In humans, the heritable deficiency of *HEXB* causes Sandhoff disease, a neurodegenerative disorder with lysosomal accumulation of lipids. Similar to the human condition, lack of *Hexb* in mice induces a fatal neurodegenerative condition accompanied by severe neurological deficits and highly activated microglia²⁶. Due to its highly enriched expression in microglia and stability during disease, we used the *Hexb* locus for the generation of two new transgenic mouse lines, namely the *Hexb*^{tdT} and *Hexb*^{CreERT2} strains. In both lines, microglial cells are morphologically, phenotypically and functionally similar to microglia in littermate controls, although the *Hexb* expression *per se* was reduced in these two lines.

Several transgenic mouse models have been generated in the past to target microglia *in vivo*⁴⁴. These models used different promoters including the Cx3cr1 promoter^{18,32,37}, the *Sall1* promoter²⁹, the human lysozyme promoter (LYZ)⁴⁵, the MHC class I promoter H-2K^b together with an immunoglobulin enhancer⁴⁶, the *Csf1r* promoter⁴⁷, the macrophage scavenger receptor type A promoter (*Msr1*)⁴⁸ and the CD11c promoter⁴⁹. So far, no transgenic lines are available that specifically target microglia while excluding CAMs in the CNS or peripheral myeloid cells, except for the *Sall1* mouse lines in which microglia, as well as the other CNS cells including astrocytes and oligodendrocytes, but not CAMs, can be targeted as we show here and has been reported previously³⁰. Indeed, the mouse lines using CX3CR1 promoter target both microglia and CAMs¹⁰.

In addition, dendritic cells and the CD11c-positive subset of microglia were both ablated in a transgenic line carrying the diphtheria toxin receptor under the control of the CD11c promoter⁴⁹ (S. Jung, unpublished observation). Similarly, a transgenic mouse model expressing HSV-TK under the control of the CD11b promoter ablated not only proliferating microglia cells on ganciclovir application but also CD11b⁺ bone marrow cells inducing hemorrhagic death in these animals⁵⁰. The power of our newly developed *Hexb*^{CreERT2} line is underscored by the specific reduction of parenchymal microglia on *Hexb*-mediated deletion of CSF1R with preservation of CAMs. On the other hand, the fact that there were still some microglia surviving in the brains of *Hexb*^{CreERT2/CreERT2}*Csf1r*^{f/f} mice might result from incomplete recombination in some cells. If so, using heterozygous flox/delta mice (*Csf1r*^{fl/fl}) crossed with *Hexb*^{CreERT2/CreERT2} mice could allow depletion of microglia more efficiently. Nevertheless, our present data underline the use of the *Hexb*^{CreERT2} line for studying the nature of microglia at both postnatal and adult stages.

We furthermore used the *Hexb*^{CreERT} line for fate mapping experiments to study the repopulation kinetics of CNS myeloid cells following BLZ945-induced depletion. It has been shown that microglia repopulation following depletion is purely based on surviving Nestin⁺ microglial cells rather than on neuroectodermal-derived cells^{32,35}. Here, we show, using the *Hexb*^{CreERT2} line, that CAMs repopulate without sharing a resident repopulating myeloid cell pool with microglia.

In sum, the inducible *Hexb*^{CreERT2} line takes advantage of unique microglia features, including the constitutive and highly restricted expression of *Hexb* and the longevity of microglia that distinguishes them from ontogenetically related CNS myeloid cells and from circulating myeloid cells in the peripheral blood. Our line is an excellent *in vivo* model that allows for the investigation of microglia-specific genes during health and disease at defined time points, opening new avenues in the exploration of microglia biology.

Online content

Any methods, additional references, Nature Research reporting summaries, source data, extended data, supplementary information, acknowledgements, peer review information; details of author contributions and competing interests; and statements of data and code availability are available at <https://doi.org/10.1038/s41590-020-0707-4>.

Received: 10 September 2019; Accepted: 7 May 2020;

Published online: 15 June 2020

References

- Colonna, M. & Butovsky, O. Microglia function in the central nervous system during health and neurodegeneration. *Annu. Rev. Immunol.* **35**, 441–468 (2017).
- Li, Q. & Barres, B. A. Microglia and macrophages in brain homeostasis and disease. *Nat. Rev. Immunol.* **18**, 225–242 (2018).
- Herz, J., Filiano, A. J., Smith, A., Yoge, N. & Kipnis, J. Myeloid cells in the central nervous system. *Immunity* **46**, 943–956 (2017).
- Priller, J. & Prinz, M. Targeting microglia in brain disorders. *Science* **365**, 32–33 (2019).
- Kierdorf, K., Masuda, T., Jordao, M. J. C. & Prinz, M. Macrophages at CNS interfaces: ontogeny and function in health and disease. *Nat. Rev. Neurosci.* **20**, 547–562 (2019).
- Prinz, M., Erny, D. & Hagemeyer, N. Ontogeny and homeostasis of CNS myeloid cells. *Nat. Immunol.* **18**, 385–392 (2017).
- Prinz, M., Jung, S. & Priller, J. Microglia biology: one century of evolving concepts. *Cell* **179**, 292–311 (2019).
- Ueno, M. et al. Layer V cortical neurons require microglial support for survival during postnatal development. *Nat. Neurosci.* **16**, 543–551 (2013).
- Hagemeyer, N. et al. Microglia contribute to normal myelinogenesis and to oligodendrocyte progenitor maintenance during adulthood. *Acta Neuropathol.* **134**, 441–458 (2017).
- Goldmann, T. et al. Origin, fate and dynamics of macrophages at central nervous system interfaces. *Nat. Immunol.* **17**, 797–805 (2016).

11. Van Hove, H. et al. A single-cell atlas of mouse brain macrophages reveals unique transcriptional identities shaped by ontogeny and tissue environment. *Nat. Neurosci.* **22**, 1021–1035 (2019).
12. Mrdjen, D. et al. High-dimensional single-cell mapping of central nervous system immune cells reveals distinct myeloid subsets in health, aging, and disease. *Immunity* **48**, 380–395 (2018).
13. Ajami, B. et al. Single-cell mass cytometry reveals distinct populations of brain myeloid cells in mouse neuroinflammation and neurodegeneration models. *Nat. Neurosci.* **21**, 541–551 (2018).
14. Bottcher, C. et al. Human microglia regional heterogeneity and phenotypes determined by multiplexed single-cell mass cytometry. *Nat. Neurosci.* **22**, 78–90 (2019).
15. Jordao, M. J. C. et al. Single-cell profiling identifies myeloid cell subsets with distinct fates during neuroinflammation. *Science* **363**, eaat7554 (2019).
16. Masuda, T. et al. Spatial and temporal heterogeneity of mouse and human microglia at single-cell resolution. *Nature* **566**, 388–392 (2019).
17. Yona, S. et al. Fate mapping reveals origins and dynamics of monocytes and tissue macrophages under homeostasis. *Immunity* **38**, 79–91 (2013).
18. Goldmann, T. et al. A new type of microglia gene targeting shows TAK1 to be pivotal in CNS autoimmune inflammation. *Nat. Neurosci.* **16**, 1618–1626 (2013).
19. Zeisel, A. et al. Cell types in the mouse cortex and hippocampus revealed by single-cell RNA-seq. *Science* **347**, 1138–1142 (2015).
20. Mildner, A. et al. Microglia in the adult brain arise from Ly-6C^{hi}CCR2⁺ monocytes only under defined host conditions. *Nat. Neurosci.* **10**, 1544–1553 (2007).
21. Butovsky, O. et al. Identification of a unique TGF-β-dependent molecular and functional signature in microglia. *Nat. Neurosci.* **17**, 131–143 (2014).
22. Zhang, Y. et al. An RNA-sequencing transcriptome and splicing database of glia, neurons, and vascular cells of the cerebral cortex. *J. Neurosci.* **34**, 11929–11947 (2014).
23. Hickman, S. E. et al. The microglial sensome revealed by direct RNA sequencing. *Nat. Neurosci.* **16**, 1896–1905 (2013).
24. Hammond, T. R. et al. Single-cell RNA sequencing of microglia throughout the mouse lifespan and in the injured brain reveals complex cell-state changes. *Immunity* **50**, 253–271 (2019).
25. Li, Q. et al. Developmental heterogeneity of microglia and brain myeloid cells revealed by deep single-cell RNA sequencing. *Neuron* **101**, 207–223 (2019).
26. Sango, K. et al. Mouse models of Tay-Sachs and Sandhoff diseases differ in neurologic phenotype and ganglioside metabolism. *Nat. Genet.* **11**, 170–176 (1995).
27. Paolicelli, R. C. et al. Synaptic pruning by microglia is necessary for normal brain development. *Science* **333**, 1456–1458 (2011).
28. Stevens, B. et al. The classical complement cascade mediates CNS synapse elimination. *Cell* **131**, 1164–1178 (2007).
29. Inoue, S., Inoue, M., Fujimura, S. & Nishinakamura, R. A mouse line expressing *Sall1*-driven inducible Cre recombinase in the kidney mesenchyme. *Genesis* **48**, 207–212 (2010).
30. Buttgeriet, A. et al. *Sall1* is a transcriptional regulator defining microglia identity and function. *Nat. Immunol.* **17**, 1397–1406 (2016).
31. Chappell-Maor, L. et al. Comparative analysis of CreER transgenic mice for the study of brain macrophages: a case study. *Eur. J. Immunol.* **50**, 353–362 (2020).
32. Bruttger, J. et al. Genetic cell ablation reveals clusters of local self-renewing microglia in the mammalian central nervous system. *Immunity* **43**, 92–106 (2015).
33. Elmore, M. R. et al. Colony-stimulating factor 1 receptor signaling is necessary for microglia viability, unmasking a microglia progenitor cell in the adult brain. *Neuron* **82**, 380–397 (2014).
34. Zhan, L. et al. Proximal recolonization by self-renewing microglia re-establishes microglial homeostasis in the adult mouse brain. *PLoS Biol.* **17**, e3000134 (2019).
35. Huang, Y. et al. Repopulated microglia are solely derived from the proliferation of residual microglia after acute depletion. *Nat. Neurosci.* **21**, 530–540 (2018).
36. Van Hove, H. et al. Identifying the variables that drive tamoxifen-independent CreERT2 recombination: implications for microglial fate mapping and gene deletions. *Eur. J. Immunol.* **50**, 459–463 (2020).
37. Tay, T. L. et al. A new fate mapping system reveals context-dependent random or clonal expansion of microglia. *Nat. Neurosci.* **20**, 793–803 (2017).
38. Fuger, P. et al. Microglia turnover with aging and in an Alzheimer's model via long-term in vivo single-cell imaging. *Nat. Neurosci.* **20**, 1371–1376 (2017).
39. Ginhoux, F. et al. Fate mapping analysis reveals that adult microglia derive from primitive macrophages. *Science* **330**, 841–845 (2010).
40. Mildner, A., Huang, H., Radke, J., Stenzel, W. & Priller, J. P2Y12 receptor is expressed on human microglia under physiological conditions throughout development and is sensitive to neuroinflammatory diseases. *Glia* **65**, 375–387 (2017).
41. Zrzavy, T. et al. Loss of 'homeostatic' microglia and patterns of their activation in active multiple sclerosis. *Brain* **140**, 1900–1913 (2017).
42. Bennett, M. L. et al. New tools for studying microglia in the mouse and human CNS. *Proc. Natl. Acad. Sci. USA* **113**, E1738–E1746 (2016).
43. Kaiser, T. & Feng, G. Tmem119-EGFP and Tmem119-CreERT2 transgenic mice for labeling and manipulating microglia. *eNeuro* **6**, ENEURO.0448–18.2019 (2019).
44. Wieghofer, P., Knobeloch, K. P. & Prinz, M. Genetic targeting of microglia. *Glia* **63**, 1–22 (2015).
45. Dighe, A. S. et al. Tissue-specific targeting of cytokine unresponsiveness in transgenic mice. *Immunity* **3**, 657–666 (1995).
46. Zehntrner, S. P., Brisebois, M., Tran, E., Owens, T. & Fournier, S. Constitutive expression of a costimulatory ligand on antigen-presenting cells in the nervous system drives demyelinating disease. *FASEB J.* **17**, 1910–1912 (2003).
47. Siao, C. J., Fernandez, S. R. & Tsirka, S. E. Cell type-specific roles for tissue plasminogen activator released by neurons or microglia after excitotoxic injury. *J. Neurosci.* **23**, 3234–3242 (2003).
48. Rong, L. L. et al. RAGE modulates peripheral nerve regeneration via recruitment of both inflammatory and axonal outgrowth pathways. *FASEB J.* **18**, 1818–1825 (2004).
49. Jung, S. et al. In vivo depletion of CD11c⁺ dendritic cells abrogates priming of CD8⁺ T cells by exogenous cell-associated antigens. *Immunity* **17**, 211–220 (2002).
50. Heppner, F. L. et al. Experimental autoimmune encephalomyelitis repressed by microglial paralysis. *Nat. Med.* **11**, 146–152 (2005).

Publisher's note Springer Nature remains neutral with regard to jurisdictional claims in published maps and institutional affiliations.

© The Author(s), under exclusive licence to Springer Nature America, Inc. 2020

Methods

Mice: generation of *Hexb*^{tdTomato} and *Hexb*^{CreERT2} mice. CRISPR/Cas9 system was used to knockin the T2A-tdTomato or T2A-CreERT2 cassette into the *Hexb* locus by injecting mouse embryos on a C57Bl/6N background with in vitro assembled CRISPR/Cas9 constructs in combination with donor-DNA generated by gene synthesis (Genescript). In both cases double strand break was directed using a single-guide RNA (sequence 5'-CCUUUAUACAGGAUCUGUAA) that was tested by transient transfection of NIH3t3 cells followed by surveyor assays. For the donor vector for the *Hexb*^{tdTomato} mouse line the sequence encoding tandem Tomato preceded by the sequence encoding a T2A self-cleavage peptide was flanked by a 680 basepair 5' and a 800 bp 3' homology region. Likewise, for the high-dynamic-range mediated integration of the CreERT2 cassette the donor vector contained the same 5' and 3' homology regions of the genomic *HexB* locus. Precise sequences for the high-dynamic-range donor vectors are available on request. Correct integration of the T2A-tdTomato or the T2A-CreERT2 cassette upstream of the *Hexb* stop codon (Figs. 3a and 6a) was confirmed by diagnostic PCR using a primer upstream of the homology (5'-CACCACAACTCTATTATGCGG-3') in combination with a reverse primer located in the T2A sequence (5'-AGGATTCTCTCGACGTCACC-3'). Sequencing of the genomic region of interest after amplification by PCR was further used to verify correct integration. On germline transmission correctly targeted founders were crossed with C57Bl/6N mice to establish the colonies for this study. For genotyping, three primers were used (1, CACCACAACTCTATTATGCGG; 2, AGGATTCTCTCGACGTC and 3, TGGAGTGTAGTGCAGG) for both *Hexb*^{tdTomato} and *Hexb*^{CreERT2} mice, which give a 1,030-bp band for wildtype control and a 830-bp band for transgenic mice (Supplementary Fig. 4a).

Additional mouse lines. C57BL/6N and CD1 mice were used as wildtype mice. Transgenic lines including *Cx3cr1*^{GFP} (B6.129P2(Cg)-*Cx3cr1*^{tm1Litt}/J), *Cx3cr1*^{CreERT2} (B6.129P2(C)-*Cx3cr1*^{tm2.1cre/ERT2}l^{fjung}/J), *Sall1*^{CreERT2} (B6.129-Sall1^{tm1(Cre)}/J), *Thy1*^{GFP} (Tg(Thy1-EGFP)MJs/J) and *Hexb*^{-/-} (B6.129S4-*Hexb*^{tm1Rip}/J) were used in this study. *Sall1*^{CreERT2} mice were kindly provided by Dr. Ryuichi Nishinakamura (Kumamoto University). All mice were bred in-house under pathogen-free conditions. *Cx3cr1*^{CreERT2}, *Sall1*^{CreERT2} and *Hexb*^{CreERT2} mice were crossed to either *R26*^{tdTomato} or *R26*^{VFP}, *Csf1r*^{fl/fl} (B6.Cg-*Csf1r*^{tm1.1jwp}/J) mice. 5xFAD transgenic mice coexpressing human APP_{K670N/M671L}(Sw)+_{I716V}(Fl)+_{V717I(Lo)} and PS1_{M146L+L280V} under the control of the neuron-specific Thy-1 promoter were used at the age of 30 weeks. All animal experiments were approved by local administration and were performed in accordance to the respective national, federal and institutional regulations.

TAM treatment. For activation of Cre recombinase, TAM (Sigma-Aldrich) was dissolved in corn oil (Sigma-Aldrich) before injection. To induce Cre recombination in neonates, pups were i.p. injected with 0.1 mg TAM/5 µl oil at postnatal day 1 (P1) and P3 (Fig. 6 and Supplementary Figs. 7–9) or with 0.4 mg TAM/20 µl oil at P7 and P9 (Figs. 6 and 7). In 5–8-week-old adult mice, Cre recombination was induced by injecting 4 mg TAM/200 µl oil i.p. twice 48 h apart (Supplementary Figs. 10 and 11). Alternatively, 5–6-week-old adult mice were injected subcutaneously with 6 mg TAM/150 µl oil for 3 d in a row (Fig. 8 and Supplementary Fig. 12).

scRNA-seq. Cells including microglia were FACS-sorted, from up to six different CNS regions of healthy and diseased brains, into a 384-well plate containing a lysis buffer and were analyzed using Smart-seq2 protocol or the Cell-Seq2 protocol and processed as previously described⁵¹. The gating strategies for FACS-sorting, related to the datasets shown in Fig. 1 and Supplementary Fig. 2, were shown in Supplementary Fig. 1, and the ones related to Fig. 2 were described previously¹⁵. Expression profiles were obtained as absolute complementary DNA molecule counts using the STAR aligner⁵² to align raw sequences in conjunction with feature counts as part of the subread package⁵³ to obtain gene counts. Further analysis and data normalization was performed using the RaceID package as previously published⁵⁴. Clusters with more than ten individual cells were retained for further analysis and normalized to ‘transcripts per million’ to compensate for differences in total transcriptome size between cell types. Additional information is provided in Supplementary Tables 1–13.

Bulk RNA-seq. Microglia were sorted using FACS from whole brains of each mouse line (see gating strategies used for FACS shown in Supplementary Fig. 1), into a collection tube and then total RNA was extracted using Picopure RNA extraction kit (Life Technologies) according to the manufacturer's protocol. The SMARTer Ultra Low Input RNA Kit for Sequencing v.4 (Clontech Laboratories, Inc.) was used to generate first strand cDNA from 500 pg total RNA. Library preparation was carried out as described in the Illumina Nextera XT Sample Preparation Guide (Illumina, Inc.). Then, 150 pg of input cDNA were fragmented (tagged and fragmented) by the Nextera XT transposome. The products were purified and amplified via a limited-cycle PCR program to generate multiplexed sequencing libraries. Equimolar amounts of each library were pooled, and the pools were used for cluster generation on the cBot with the Illumina TruSeq SR Cluster Kit v.3. The sequencing run was performed either on a HiSeq 1000 instrument using the indexed, 50 cycles of single-read protocol and the TruSeq

SBS v.3 Reagents according to the Illumina HiSeq 1000 System User Guide, or on a NextSeq 500 instrument controlled by the NextSeq Control Software v.2.2.0, using a 75 Cycles High Output Kit with the dual index, single-read run parameters. Image analysis and base calling resulted in bcl files, which were converted into fastq files with either the CASAVA1.8.2 software or with the bcl2fastq v.2.18 software. RNA isolation, library preparation and RNA-seq were performed at the Genomics Core Facility, KFB (Center of Excellence for Fluorescent Bioanalytics, University of Regensburg, Regensburg, Germany).

Flow cytometry. After transcardial perfusion with PBS, brains were roughly minced and homogenized with a Potter tissue grinder in Hanks' balanced salt solution containing 15 mM HEPES buffer and 0.54% glucose. Whole brain homogenate was separated by 37% Percoll gradient centrifugation at 800g for 30 min at 4°C (no brake). The pellet containing CNS macrophages at the bottom of the tube was then collected and washed once with PBS containing 2% FCS and 10 mM EDTA before staining. For the analysis of macrophages in kidney, liver and spleen, the organs were cut in small pieces using scissors and digested for 30 min at 37°C in 1 ml PBS supplemented with 3% FCS, 5 mg ml⁻¹ DNase 1 (Sigma-Aldrich, DN25-100MG) and 5 mg ml⁻¹ Collagenase D (Roche, 11088866001). Following digestion, the tissues were homogenized through a 100 µm cell strainer (Corning, 352360) and single cells were collected in FACS buffer. Liver samples were then centrifuged for 3 min at 30g to remove hepatocytes and the supernatant was used for further analysis. The single-cell suspension was used for the staining procedure as described.

Fc receptors were blocked with Fc Block (2.4G2, BD Biosciences) for 10 min at 4°C before incubation with the primary antibodies. Cells were stained with antibodies directed against CD11b (M1/70, BioLegend), CD45 (30-F11, ThermoFisher Scientific), Ly6C (AL-21, BD Biosciences), Ly6G (1A8, BD Biosciences), CD115 (AFS98, ThermoFisher Scientific), CD11c (N418, ThermoFisher Scientific), MHC class II (M5/114.15.2, ThermoFisher Scientific), Tim-4 (RMT4-54, BioLegend), CD3e (eBio500A2, ThermoFisher Scientific), CD19 (eBio1D3, ThermoFisher Scientific) and CD206 (C068C2, BioLegend) for 45 min at 4°C. After washing, cells were sorted using a MoFlo Astrios (Beckman Coulter) or analyzed using a BD LSRFortessa (Becton Dickinson). Viable cells were gated by staining with Fixable Viability Dye (65-0866, eBioscience) or 4,6-diamidino-2-phenylindole (DAPI). For the quantification of kidney macrophages, 50 µl of AccuCheck Counting Beads (ThermoFisher, PCB100) were added to each sample before flow cytometric analysis. Total macrophage counts per liver were determined by normalizing the recorded cell counts for each sample by calculating the ratio of recorded AccuCheck beads to total beads added according to the manufacturer's instructions. Data were acquired with FACSDiva software (Becton Dickinson). Postacquisition analysis was performed using FlowJo software, v.10.5.3.

Immunohistochemistry and cell quantifications. After transcardial perfusion with PBS, brains were fixed for 5 h in 4% PFA, dehydrated in 30% sucrose and embedded in Tissue-Tek O.C.T. compound (Sakura Finetek). Cryosections were obtained as described previously⁵⁵. Next, 20 µm (only for the quantification of cell density) or 30 µm sections were blocked with PBS containing 5% bovine serum albumin and permeabilized with 0.5% Triton-X 100 in blocking solution. Primary antibodies were added over night at a dilution of 1:1,000 for Iba1 (ab178846, Abcam; 234004, Synaptic Systems), 1:200 for CD206 (MCA2235, Biorad), 1:200 for collagen IV (AB769, Millipore), 1:500 for NeuN (MAB377, Millipore), 1:500 for APC (OB80, Millipore), 1:500 for YFP (ab13970, Abcam), 1:500 for SOX9 (AF3075, R&D), 1:500 for P2Y12R (AS-55043A, Anaspec), 1:500 for Ki-67 (ab15580, abcam), 1:500 for cleaved caspase3 (559565, BD Biosciences) and 1:500 for F4/80 (clone:BM8, Biologend) at 4°C. Secondary antibodies were purchased from Thermo Fisher Scientific added as follows: Alexa Flour 405 1:1,000, Alexa Flour 488 1:1,000, Alexa Flour 568 1:1,000 and Alexa Fluor 647 1:1,000 for 2 h at room temperature. Coverslips were mounted with/without ProLong Diamond Antifade Mountant with/without DAPI (Thermo Fisher Scientific). Images were taken using a conventional fluorescence microscope (Olympus BX-61 with a color camera (Olympus DP71) or BZ-9000 (Keyence) and the confocal pictures were taken with Fluoview FV 1000 (Olympus) using a ×20 1.0 numerical aperture (NA) (XLUMPlanFL N, Olympus) or with a TCS SP8 X (Leica) using a ×20 0.75 NA (HC PL APO ×20/0.75 NA IMM CORR CS2). To assess density of cells, numbers of Iba1⁺ CD206⁺ (microglia) or CD206⁺ cells (pvMΦ and mMΦ) were quantified on a wide field microscope (BZ-9000). Microglia and pvMΦ were normalized to the area of the region of interest and expressed as cells per mm². mMΦ were normalized to the length of the leptomeninges indicated by collagen IV immunofluorescence and finally expressed as cells per mm. To assess proportion of cells that are positive for Ki-67, cleaved caspase3 or P2RY12, only Iba1⁺CD206⁺ microglia are analyzed. To assess labeling efficacy for YFP, GFP or tdTomato, Iba1⁺CD206⁺ microglia, CD206⁺ pvMΦ and mMΦ, SOX9⁺ astrocytes, NeuN⁺ neurons, APC⁺ oligodendrocytes were counted and analyzed. At least three sections of a minimum of four mice were used for each analysis.

FNX and cuprizone model of de- and remyelination. Facial nerve was injured as described previously^{20,37}. Briefly, mice were anesthetized by subcutaneous injection of a mixture of ketamine (50 mg kg⁻¹) and xylazine (7.5 mg kg⁻¹), and the right

facial nerve was transected at the stylomastoid foramen, resulting in ipsilateral whisker paresis. Cuprizone treatment was used as a model of toxic, demyelination and remyelination^{30,56}. For demyelination, mice were fed for 5 weeks with 0.45% (wt/wt) cuprizone (Sigma) in the ground breeder chow. For remyelination, the cuprizone diet was discontinued after 5 weeks and animals were maintained for further 5 weeks under normal diet to allow spontaneous remyelination. Untreated age-matched mice were used as control.

EAE. For the induction of EAE, mice were immunized subcutaneously with 200 µg of MOG_{35–55} peptide emulsified in Complete Freund's Adjuvant containing 0.1 mg of Mycobacterium tuberculosis (H37RA; Difco Laboratories) as described before^{57,58}. The mice received intraperitoneal (i.p.) injections with 250 ng of pertussis toxin (Sigma-Aldrich) at the time of immunization and 48 h later. For experiments involving C57BL/6 and *Hexb^{tdTomato}* mice, immunizations were performed in 6–8-week-old mice. Mice were scored daily according to their clinical symptoms (score 1, complete limp tail; score 1.5, limp tail and hindlimb weakness; score 2, hindlimb paresis; score 2.5, unilateral hindlimb paralysis; score 3, bilateral hindlimb paralysis). For the EAE experiments presented in this study, mice were analyzed at the preclinical phase (day 8 after immunization), onset phase (score 1, typically observed between day 11–13), peak phase (score 3, typically observed between days 15 and 20) or at the chronic phase (day 30 postimmunization) of EAE.

In vivo imaging of microglia under steady conditions and after laser ablation. To image the movement of microglia processes, animal were anesthetized via i.p. injection of ketamine (100 mg kg⁻¹ body weight) and xylazine (10 mg kg⁻¹ body weight) or with a mixture of medetomidin (0.5 mg kg⁻¹), midazolam (5 mg kg⁻¹) and fentanyl (0.05 mg kg⁻¹) and a 3-mm cranial window was implanted over the somatosensory cortex of 12–16 week-old *Cx3cr1^{GFP}* or *Hexb^{tdT}* mice. After the craniotomy, mice were kept anesthetized for all the duration the imaging, and the body temperature was maintained at 36–37 °C using a heating blanket. Depth of anesthesia was assessed by monitoring pinch withdrawal, respiration rate and vibrissae movements. Laser lesion and the acute two-photon imaging were carried out using Olympus FV1000 with Mai Tai Deep See Laser (Spectra Physics, Newport Corporation) with an excitation wavelength of 900 nm to visualize the GFP or FV-RS Olympus 2P microscope using InSight 2P laser (Newport) at 1,050 nm to visualize the tdTomato. The images shown in Fig. 5b were acquired with resonant scanner with a pixel size of 0.5 µm (×2 zoom) and 0.25 µm (×4 zoom). A 900 nm-focused laser injury was induced at a small area of about 80 µm² within the region of interest at 50 µm below the pial surface using an increment of power laser of 75–80% for 30 s with a frequency of 8 pixels per µs. Microglia response was then recorded every 5 min for a total of 35 min at a depth range of 30–70 µm with 2.5-µm z-increments and a 512 × 512 pixel resolution. In each mouse, four to six different laser ablations were performed. The same acquisition parameters were used to image microglia process under normal condition. For the quantification of process movement, the extension of individual processes was tracked manually and measured using ImageJ software (<https://imagej.nih.gov/ij/>), considering the initial (at *t*=0 min) and the final distance (at *t*=35 min) from the center of the laser lesion. The mean speed and distance traveled were calculated for each microglial process. The percentage of responsive microglial cells were quantified by counting the cells that showed at least one process moving toward the lesion site. The position of the different processes at *t*=0 min was divided in four different ranges: 0–30, 31–60, 61–90 and 91–120 µm.

Ex vivo imaging. Entorhino-hippocampal tissue cultures were prepared at postnatal days 4–5 from *Thy1^{GFP}* × *HexB^{tdT}* mice of either sex. Cultivation medium contained 50% (v/v) MEM, 25% (v/v) basal medium eagle, 25% (v/v) heat-inactivated normal horse serum, 25 mM HEPES buffer solution, 0.15% (w/v) bicarbonate, 0.65% (w/v) glucose, 0.1 mg ml⁻¹ streptomycin, 100 U ml⁻¹ penicillin and 2 mM glutamax. The pH was adjusted to 7.3 and the medium was replaced three times per week. All slice cultures were allowed to mature for at least 14 d in humidified atmosphere with 5% CO₂ at 35 °C. Imaging was performed at a Zeiss LSM800 confocal scanning microscope. The bath solution contained 60% (v/v) MEM, 40% (v/v) basal medium eagle, 75 mM HEPES buffer solution, 0.15% (w/v) bicarbonate, 0.65% (w/v) glucose and 2 mM glutamax (pH 7.3 under continuous oxygenation with 5% CO₂/95% O₂). Confocal image stacks (z-step size, 0.5 µm; ideal Nyquist rate) were acquired every minute with a ×40 objective lens (1.0 NA, water immersion, Zeiss) over a 20-min time frame. Microglia end tips and microglia/neuron-contact sites were analyzed manually using the ImageJ software package (<https://imagej.nih.gov/ij/>).

CSF1 receptor inhibitor BLZ945 treatment. The BLZ945 (kindly provided by Novartis) was dissolved in 20% (2-hydroxypropyl)-β-cyclodextrin (Sigma-Aldrich). A dose of 200 mg kg⁻¹ bodyweight was used. In adult (6–7 week-old) mice, BLZ945 was applied by oral gavage for seven consecutive days 1 week after the first

TAM application. The mice were analyzed 14 d after the last application of TAM or vehicle.

Statistical analysis. Statistical significance was determined using Student's *t*-test or one-way analysis of variance (ANOVA) with post hoc Tukey multiple comparison test using GraphPad Prism v.5.04 software. Further details on statistics used during analysis of RNA-sequencing data are provided in the method section and the Life Sciences Reporting summary.

Reporting Summary. Further information on research design is available in the Nature Research Reporting Summary linked to this article.

Data availability

Raw data for new scRNA-seq or bulk RNA-seq have been deposited in the Gene Expression Omnibus, and are available at the following accession numbers: GSE148405 (scRNA-seq) and GSE148413 (bulk RNA-seq). All other data are published previously or are available from the corresponding authors on reasonable request.

References

51. Hashimshony, T. et al. CEL-Seq2: sensitive highly-multiplexed single-cell RNA-seq. *Genome Biol.* **17**, 77 (2016).
52. Dobin, A. et al. STAR: ultrafast universal RNA-seq aligner. *Bioinformatics* **29**, 15–21 (2013).
53. Liao, Y., Smyth, G. K. & Shi, W. The Subread aligner: fast, accurate and scalable read mapping by seed-and-vote. *Nucleic Acids Res.* **41**, e108 (2013).
54. Herman, J. S., Sagar, & Grun, D. FateID infers cell fate bias in multipotent progenitors from single-cell RNA-seq data. *Nat. Methods* **15**, 379–386 (2018).
55. Goldmann, T. et al. USP18 lack in microglia causes destructive interferonopathy of the mouse brain. *EMBO J.* **34**, 1612–1629 (2015).
56. Raasch, J. et al. IκB kinase 2 determines oligodendrocyte loss by non-cell-autonomous activation of NF-κB in the central nervous system. *Brain* **134**, 1184–1198 (2011).
57. Dann, A. et al. Cytosolic RIG-I-like helicases act as negative regulators of sterile inflammation in the CNS. *Nat. Neurosci.* **15**, 98–106 (2012).
58. Prinz, M. et al. Distinct and nonredundant in vivo functions of IFNAR on myeloid cells limit autoimmunity in the central nervous system. *Immunity* **28**, 675–686 (2008).

Acknowledgements

We thank E. Barleon for excellent technical assistance and the Center for Animal Resource and Development (CARD, Kumamoto University) for providing research material. T. Masuda was supported by the KANAE Foundation for the Promotion of Medical Science and the Japan Society for the Promotion of Science (JSPS) as the JSPS Postdoctoral Fellow for Research Abroad. M.P. was supported by the Sobek Foundation, the Ernst-Jung Foundation, the German Research Foundation (DFG) (grant nos. SFB 992, SFB1160, SFB/TRR167, Reinhart-Koselleck-Grant and the Gottfried Wilhelm Leibniz-Prize) and the Ministry of Science, Research and Arts, Baden-Wuerttemberg (Sonderlinie 'Neuroinflammation'). This study was supported by the DFG under Germany's Excellence Strategy (grant no. CIBSS—EXC-2189, Project ID390939984). J.P. was supported by the DFG (grant nos. SFB/TRR167 B05 and B07), and the UK DRI Momentum Award. C.B. was supported by the DFG (grant no. SFB/TRR167 B05).

Author contributions

T. Masuda, L.A., P.E., M.L., N.S., T. Misgeld, R.S., O.S., M.J.C.J., C.B., K.K., D.G., A.V. and K.P.K. conducted experiments and analyzed the data. M.P., K.P.K., S.J., M.M.L. and J.P. analyzed the data, contributed to the in vivo studies and provided mice or reagents. T. Masuda and M.P. supervised the project and wrote the manuscript, J.P. edited the manuscript.

Competing interests

The authors declare no competing interests.

Additional information

Supplementary information is available for this paper at <https://doi.org/10.1038/s41590-020-0707-4>.

Correspondence and requests for materials should be addressed to T.M. or M.P.

Reprints and permissions information is available at www.nature.com/reprints.

Editor recognition statement Zoltan Fehervari was the primary editor on this article and managed its editorial process and peer review in collaboration with the rest of the editorial team.

Reporting Summary

Nature Research wishes to improve the reproducibility of the work that we publish. This form provides structure for consistency and transparency in reporting. For further information on Nature Research policies, see [Authors & Referees](#) and the [Editorial Policy Checklist](#).

Statistics

For all statistical analyses, confirm that the following items are present in the figure legend, table legend, main text, or Methods section.

n/a Confirmed

- The exact sample size (n) for each experimental group/condition, given as a discrete number and unit of measurement
- A statement on whether measurements were taken from distinct samples or whether the same sample was measured repeatedly
- The statistical test(s) used AND whether they are one- or two-sided
Only common tests should be described solely by name; describe more complex techniques in the Methods section.
- A description of all covariates tested
- A description of any assumptions or corrections, such as tests of normality and adjustment for multiple comparisons
- A full description of the statistical parameters including central tendency (e.g. means) or other basic estimates (e.g. regression coefficient) AND variation (e.g. standard deviation) or associated estimates of uncertainty (e.g. confidence intervals)
- For null hypothesis testing, the test statistic (e.g. F , t , r) with confidence intervals, effect sizes, degrees of freedom and P value noted
Give P values as exact values whenever suitable.
- For Bayesian analysis, information on the choice of priors and Markov chain Monte Carlo settings
- For hierarchical and complex designs, identification of the appropriate level for tests and full reporting of outcomes
- Estimates of effect sizes (e.g. Cohen's d , Pearson's r), indicating how they were calculated

Our web collection on [statistics for biologists](#) contains articles on many of the points above.

Software and code

Policy information about [availability of computer code](#)

Data collection

STAR (version 2.5.2b) for sequence mapping/alignment to the mouse genome: <https://github.com/alexdobin/STAR>
Gencode M11 available from <https://www.gencodegenes.org/>

featurecounts (version 1.5.1) for determination of gene count, available from
<http://subread.sourceforge.net/>

NextSeq Control Software (NCS) v2.2.0 to control NextSeq 500 instrument

FV10-ASW Ver.4.2a was used for confocal imaging with the Olympus FV 1000

LAS X software was used for confocal imaging with the Leica TCS SP8 X

Data analysis

RaceID/StemID for clustering and other single cell data analysis available from <https://github.com/dgrun/StemID>

Data presentation (tsne plots, heatmaps):
R (version 3.4.3), ggplot2 (version 2.2.1) and gplots (version 3.0.1) were used available from <https://cran.r-project.org/> (R), <https://www.bioconductor.org/> (ggplot2, qplots)

CASAVA1.8.2 or bcl2fastq v2.18 were used to convert .bcl files into fastq files

GraphPad Prism 5.04 was used for statistical analysis

ImageJ software package (<https://imagej.nih.gov/ij/>) was used to analyze microglia movements in ex vivo and in vivo imaging

For manuscripts utilizing custom algorithms or software that are central to the research but not yet described in published literature, software must be made available to editors/reviewers. We strongly encourage code deposition in a community repository (e.g. GitHub). See the Nature Research [guidelines for submitting code & software](#) for further information.

Data

Policy information about [availability of data](#)

All manuscripts must include a [data availability statement](#). This statement should provide the following information, where applicable:

- Accession codes, unique identifiers, or web links for publicly available datasets
- A list of figures that have associated raw data
- A description of any restrictions on data availability

All data are available from the corresponding author on reasonable request or have been linked in the data availability statement.

Field-specific reporting

Please select the one below that is the best fit for your research. If you are not sure, read the appropriate sections before making your selection.

Life sciences Behavioural & social sciences Ecological, evolutionary & environmental sciences

For a reference copy of the document with all sections, see nature.com/documents/nr-reporting-summary-flat.pdf

Life sciences study design

All studies must disclose on these points even when the disclosure is negative.

Sample size

No statistical methods were used to predetermine sample sizes. We ensured that they were similar to those generally employed in the field.

Data exclusions

Samples, for single-cell sequencing related to Fig.1,2 and Supplementary Fig.2,3, that failed during library preparation or had very low counts (less than 5000 reads mapped to mouse genes) were excluded. Also samples with no detectable Hexb (less than 10 counts) were excluded. No other exclusions were made. Exclusion criteria for scRNAseq have been pre established in previous studies.

Replication

To be sure the reproducibility of the experimental findings, we have used at least 3 individual mice from at least two independent experiments for each sample group. All replications were successful.

Randomization

For all experiments, mice used were randomly allocated into each experimental group by TM and LA.

Blinding

Blinding was not applied in this study. Most quantifications were performed independently by TM and LA by two different methods (IF and FC).

Reporting for specific materials, systems and methods

We require information from authors about some types of materials, experimental systems and methods used in many studies. Here, indicate whether each material, system or method listed is relevant to your study. If you are not sure if a list item applies to your research, read the appropriate section before selecting a response.

Materials & experimental systems

n/a	Involved in the study
<input type="checkbox"/>	<input checked="" type="checkbox"/> Antibodies
<input checked="" type="checkbox"/>	<input type="checkbox"/> Eukaryotic cell lines
<input checked="" type="checkbox"/>	<input type="checkbox"/> Palaeontology
<input type="checkbox"/>	<input checked="" type="checkbox"/> Animals and other organisms
<input checked="" type="checkbox"/>	<input type="checkbox"/> Human research participants
<input checked="" type="checkbox"/>	<input type="checkbox"/> Clinical data

Methods

n/a	Involved in the study
<input checked="" type="checkbox"/>	<input type="checkbox"/> ChIP-seq
<input type="checkbox"/>	<input checked="" type="checkbox"/> Flow cytometry
<input checked="" type="checkbox"/>	<input type="checkbox"/> MRI-based neuroimaging

Antibodies

Antibodies used

For flow cytometry:

- anti-CD11b 1:300 (Clone M1/70, BioLegend, Cat# 101237)
- anti-CD45 1:300 (Clone 30-F11, ThermoFisher Scientific, Cat# 47-0451-82)
- anti-Ly6C 1:200 (Clone AL-21, BD Biosciences, Cat# 561237)
- anti-Ly6G 1:300 (Clone 1A8, BD Biosciences, Cat# 563978)
- anti-CD115 1:200 (Clone AFS98, ThermoFisher Scientific, Cat# 12-1152-82)
- anti-CD11c 1:300 (Clone N418, ThermoFisher Scientific, Cat# 25-0114-82)
- anti-CD3e 1:300 (Clone eBio500A2, ThermoFisher Scientific, Cat# 48-0033-82)
- anti-CD19 1:200 (Clone eBio1D3, ThermoFisher Scientific, Cat# 48-0193-82)
- anti-CD206 1:200 (Clone C068C2, BioLegend, Cat# 141708)
- anti-Tim-4 1:200 (Clone RMT4-54, BioLegend, Cat# 130008)
- anti-MHCII 1:300 (Clone M5/114.15.2, BioLegend, Cat# 107630)

For histological analysis:

- anti-Iba1 1:1000 (Abcam, Cat# ab178846; Synaptic Systems, Cat# 234004)
- anti-CD206 1:500 (Clone MR5D3, Bio Rad, Cat# MCA2235)
- anti-collagen IV 1:200 (Millipore, Cat# AB769)
- anti-Neun 1:500 (Clone A60, Millipore, Cat# MAB377)
- anti-APC 1:500 (Clone CC-1, Millipore, Cat# OB80)
- anti-YFP 1:500 (Abcam, Cat# ab13970)
- anti-SOX9 1:500 (R&D, Cat# AF3075)
- anti-P2Y12R 1:500 (Anaspec, Cat# AS-55043A)
- anti-Ki-67 1:500 (Abcam, Cat# ab15580)
- anti-cleaved caspase3 1:500 (Clone C92-605, BD Biosciences, Cat# 559565)
- anti-F4/80 1:500 (Clone BM8, Biolegend, Cat# 123102)

Various lots of each antibody have been used throughout the study. In experiments where mean fluorescence intensities were directly compared between samples (Fig. 8), the same antibody aliquot (i.e. also the same lot) was used for all samples. The same applies to all histological analysis were multiple animals have been compared.

Validation

All primary anti-mouse antibodies used in flow cytometry antibodies have been validated for this application by the supplier and have been used in previous studies. Selected references and validations for each antibody can be found online under the respective catalog numbers.

All primary antibodies used in immunofluorescence microscopy have been validated for this application by the supplier and/or have been used in previous studies. Selected references and validations for each antibody can be found online under the respective catalog numbers.

Animals and other organisms

Policy information about [studies involving animals](#); [ARRIVE guidelines](#) recommended for reporting animal research

Laboratory animals

For all scRNASeq datasets and for EAE experiments, only female mice were used. For all other experiments, mice of both genders were used. HexbtdTomato and HexbCreERT2 mice were generated as described in the Methods and were used in this study. C57BL/6 and CD1 mice were used as wild-type mice. Transgenic lines including Cx3cr1GFP (B6.129P2(Cg)-Cx3cr1tm1Litt/J), Cx3cr1CreERT2 (B6.129P2(C)-Cx3cr1tm2.1(cre/ERT2)Jung/J), Sall1CreERT2 (B6.129-Sall1tm1(Cre)), Thy1GFP (Tg(Thy1-EGFP)Mjrs/J), Hexb-/- (B6.129S4-Hexbtm1Rlp/J) were used in this study. All mice were bred in-house under pathogen-free conditions. Cx3cr1CreERT2, Sall1CreERT2 and HexbCreERT2 mice were crossed to either R26tdTomato or R26YFP, Csf1rflox (B6.Cg-Csf1rtm1.1Jwp/J) mice. 5xFAD transgenic mice coexpressing human APPK670N/M671L (Sw)+T716V (Fl)+V717I(Lo) and PS1M146L+L286V under the control of the neuron-specific Thy-1 promoter were used at the age of 30 weeks. The age of all other experimental animals is provided in each figure legend.

Wild animals

This study did not involve wild animals.

Field-collected samples

This study did not involve field-collected samples.

Ethics oversight

An ethics statement is provided in the methods section. The local authorities (Regierungspräsidium Freiburg) have approved animal experiments.

Note that full information on the approval of the study protocol must also be provided in the manuscript.

Flow Cytometry

Plots

Confirm that:

- The axis labels state the marker and fluorochrome used (e.g. CD4-FITC).
- The axis scales are clearly visible. Include numbers along axes only for bottom left plot of group (a 'group' is an analysis of identical markers).
- All plots are contour plots with outliers or pseudocolor plots.
- A numerical value for number of cells or percentage (with statistics) is provided.

Methodology

Sample preparation

After transcardial perfusion with PBS, brains were roughly minced and homogenized with a potter tissue grinder in HBSS containing 15 mM HEPES buffer and 0.54 % glucose. Whole brain homogenate was separated by 37 % Percoll gradient centrifugation at 800 g for 30 min at 4 °C (no brake). The pellet containing CNS macrophages at the bottom of the tube was then collected and washed once with PBS containing 2 % FCS and 10mM EDTA before staining. FC receptors were blocked with Fc Block (2.4G2, BD Biosciences) for 10 min at 4 °C prior to incubation with the primary antibodies. Cells were stained with antibodies directed against CD11b (M1/70, BioLegend), CD45 (30-F11, BD Biosciences), Ly6C (AL-21, BD Biosciences), Ly6G (1A8, BD Biosciences), CD115 (AFS98, ThermoFisher Scientific), CD11c (N4A18, ThermoFisher Scientific), CD3e (eBio500A2, ThermoFisher Scientific), CD19 (eBio1D3, ThermoFisher Scientific) and CD206 (C068C2, BioLegend) for 45 min at 4 °C.

Instrument

Cells were sorted using a MoFlo Astrios (Beckman Coulter) or analyzed using a BD LSRFortessa (Becton Dickinson)

Software

Data were acquired with FACSDiva software (Becton Dickinson). Postacquisition analysis was performed using FlowJo software, version 10.5.3.

Cell population abundance

N.A.

Gating strategy

In all experiments, small debris was removed with the preliminary FSC/SSC gate. Single, living cells were obtained by doublet exclusion and exclusion of dead cells with live-dead dyes or DAPI. Hematopoietic cells were defined by CD45 expression and positive and negative staining populations were defined using isotype controls if necessary.

- Tick this box to confirm that a figure exemplifying the gating strategy is provided in the Supplementary Information.